



LAWRENCE
LIVERMORE
NATIONAL
LABORATORY

EXTREMELY NA- AND CL-RICH CHONDRULE FROM THE CV3 CARBONACEOUS CHONDRITE ALLENDE

G. J. Wasserburg, I. D. Hutcheon, J. Aleon, E. C.
Ramon, A. N. Krot, K. Nagashima, A. J. Brearley

January 27, 2011

Geochimica et Cosmochimica Acta

Disclaimer

This document was prepared as an account of work sponsored by an agency of the United States government. Neither the United States government nor Lawrence Livermore National Security, LLC, nor any of their employees makes any warranty, expressed or implied, or assumes any legal liability or responsibility for the accuracy, completeness, or usefulness of any information, apparatus, product, or process disclosed, or represents that its use would not infringe privately owned rights. Reference herein to any specific commercial product, process, or service by trade name, trademark, manufacturer, or otherwise does not necessarily constitute or imply its endorsement, recommendation, or favoring by the United States government or Lawrence Livermore National Security, LLC. The views and opinions of authors expressed herein do not necessarily state or reflect those of the United States government or Lawrence Livermore National Security, LLC, and shall not be used for advertising or product endorsement purposes.

EXTREMELY NA- AND CL-RICH CHONDRULE FROM THE CV3 CARBONACEOUS CHONDRITE ALLENDE

Dedicated to the memory of Brian Mason

G. J. Wasserburg¹, I. D. Hutcheon², J. Aléon³, E. C. Ramon², A. N. Krot⁴, K. Nagashima⁴, and A.
J. Brearley⁵

¹California Institute of Technology, MC 170-25, Pasadena, CA 91125, USA

²Glenn Seaborg Institute, Lawrence Livermore National Laboratory, Livermore, CA 94551, USA

³CSNSM IN2P3-CNRS, Batiment 104, 91405 Orsay Campus, France

⁴Hawai'i Institute of Geophysics and Planetology, School of Ocean, Earth Science and
Technology, University of Hawai'i at Manoa, Honolulu, HI 96822, USA

⁵University of New Mexico, Albuquerque, NM 87131, USA

Abstract. We report on a study of *Al3509*, a large Na- and Cl-rich, radially-zoned object from the oxidized CV carbonaceous chondrite Allende. *Al3509* consists of fine-grained ferroan olivine, ferroan high-Ca pyroxene, nepheline, sodalite, and andradite, and is crosscut by numerous veins of nepheline, sodalite, and ferroan high-Ca pyroxene. Some poorly-characterized phases of fine-grained material are also present; these phases contain no significant H₂O. The listed minerals are commonly found in Allende CAIs and chondrules and are attributed to late-stage iron-alkali-halogen metasomatic alteration of primary high-temperature minerals. Textural observations indicate that *Al3509* is an igneous object. No residual crystals that might be relicts of pre-existing CAI or chondrule minerals were identified. To establish the levels of ²⁶Al and ³⁶Cl originally present, ²⁶Al-²⁶Mg and ³⁶Cl-³⁶S isotopic systematics in sodalite were investigated. *Al3509* shows no evidence of radiogenic ²⁶Mg*, establishing an upper limit of the initial ²⁶Al/²⁷Al ratio of 3×10⁻⁶. All sodalite grains measured show large but variable excesses of ³⁶S, however, there is no correlation of ³⁶S/³⁴S with ³⁵Cl/³⁴S. If these excesses are due to decay of ³⁶Cl, local redistribution of radiogenic ³⁶S* after ³⁶Cl had decayed is required. The oxygen-isotope pattern in *Al3509* is the same as found in secondary minerals resulting from iron-alkali-halogen metasomatic alteration of Allende CAIs and chondrules and in melilite and anorthite of most CAIs in Allende. The oxygen-isotope data suggests that the secondary minerals precipitated

from or equilibrated with a fluid of similar oxygen isotopic composition. Hydrothermal reaction products are present only in trace amounts in *Al3509*. These observations suggest that the formation of *Al3509* and alteration products in CAIs and chondrules in Allende requires a very similar fluid phase, greatly enriched in volatiles (e.g., Na and Cl). The fundamental problem of obtaining large concentrations of the volatiles Na and Cl remains a central issue. We argue that internal heating of even small planetesimals by ^{26}Al would efficiently transfer volatiles to their outer portions and enhance the formation of minerals highly enriched in volatiles and conclude that the site for the production of Na- and Cl-rich fluids responsible for the formation of *Al3509* and the alteration of the Allende CAIs and chondrules must have occurred on a protoplanetary body prior to incorporation into the Allende meteorite.

INTRODUCTION

We report on the mineralogy, petrology, chemistry, oxygen isotopes, ^{26}Al - ^{26}Mg and ^{36}Cl - ^{36}S isotope systematics of a large Al-rich chondrule, *Al3509*, from the Allende meteorite, which is extremely rich in Na (~10 wt%) and Cl (~1 wt%). This very volatile-rich object was discovered by Clarke et al. (1970). The major phases were identified as ferroan olivine (Fa_{26}), nepheline, sodalite, and ferroan Al-diopside (Mason and Taylor, 1982). Mason and Martin (1977) determined minor and trace elements of *Al3509*; the concentrations of rare earth elements are at about chondritic level, but with a positive Eu anomaly ($\text{Eu}/\text{Eu}^* = 2.9$). Wasserburg and Huneke (1979) showed that this halogen-rich object is extremely enriched in ^{129}Xe , produced by decay of ^{129}I ($t_{1/2} \sim 15.7$ Myr), with an initial $^{129}\text{I}/^{127}\text{I}$ ratio of 1.1×10^{-4} , in accord with the levels first reported by Reynolds (1967) in typical chondrites (Wasserburg, 1985).

The high enrichment of halogens in *Al3509* makes it important in searching for excess radiogenic ^{36}S from the decay of ^{36}Cl ($t_{1/2} \sim 0.3$ Myr). Excesses of ^{36}S correlated with $^{35}\text{Cl}/^{34}\text{S}$ ratios have been reported in sodalite ($\text{Na}_8\text{Al}_6\text{Si}_6\text{O}_{24}\text{Cl}_2$) replacing melilite, plagioclase or glassy mesostasis in calcium-aluminum-rich inclusions (CAIs) and chondrules from the Allende (CV) and Ningqiang (CV anomalous) carbonaceous chondrites and provide strong evidence for the *in situ* decay of ^{36}Cl (Lin et al., 2005; Hsu et al., 2006; Ushikubo et al., 2007; Nakashima et al., 2008). While these studies demonstrate unequivocally that ^{36}Cl was extant in the early solar system, they do not explain the absence of large correlated effects in ^{36}Ar that would be expected, as 98.1% of ^{36}Cl decays to ^{36}Ar . Existing data also fail to constrain the initial

abundance of ^{36}Cl , because not all sodalite grains within a CAI or a chondrule are found to show ^{36}S excesses correlated with $^{35}\text{Cl}/^{34}\text{S}$ ratios; some sodalite grains show no resolvable ^{36}S excess (Nakashima et al., 2008). The highest value of the inferred initial $^{36}\text{Cl}/^{35}\text{Cl}$ ratio reported in CV sodalite is $\sim 4 \times 10^{-6}$. Recently, Jacobsen et al. (2009) and Matzel et al. (2010) reported evidence for a much higher initial abundance of ^{36}Cl in wadalite $[\text{Ca}_6(\text{Al},\text{Si},\text{Mg})_7\text{O}_{16}\text{Cl}_3]$ in the Allende Type B inclusion *AJEF*. For Type B CAIs, the inferred initial $^{36}\text{Cl}/^{35}\text{Cl}$ in wadalite ranges from $\sim 2 \times 10^{-5}$ in *AJEF* to $\sim 3 \times 10^{-7}$ in *Egg-6* and *TS34*. In these CAIs, wadalite together with grossular, monticellite, Al-rich pyroxene, wollastonite, and Na-rich melilite replace åkermanitic melilite and anorthite in cores of the inclusions. Sodalite together with nepheline, secondary anorthite, and ferroan olivine replaces gehlenitic melilite and anorthite in CAI mantles and Wark-Lovering rims (Ishii et al., 2010; Krot et al., 2010).

Observations show that ^{36}Cl - ^{36}S and ^{26}Al - ^{26}Mg systematics in CV CAIs are not correlated indicating that the production mechanisms of ^{36}Cl and ^{26}Al are different (Lin et al., 2005; Hsu et al., 2006). From the inferred $^{36}\text{Cl}/^{35}\text{Cl}$ ratios and consideration of both asymptotic giant branch (AGB) star and supernova (SN) sources, ^{36}Cl must be produced by charged particle bombardment from the early Sun (Hsu et al., 2006). Based on the mineralogy, petrography, O-isotope compositions, ^{26}Al - ^{26}Mg and ^{36}Cl - ^{36}S ratios of the secondary mineralization in the Allende CAIs, short-lived ^{36}Cl is inferred to have been present in volatile-rich zones of protoplanets (Jacobsen et al., 2009; Matzel et al., 2010; Krot et al., 2010). The specific means of production of ^{36}Cl and the site of the irradiation have not yet been identified.

In all known cases, evidence for ^{36}Cl has only been found in secondary sodalite and wadalite replacing pre-existing primary minerals in both CAIs and ferromagnesian chondrules. The nature of the widespread volatile-rich alteration process remains controversial; two classes of models, asteroidal and nebular, are currently being discussed (e.g., Hashimoto and Grossman, 1987; Palme and Wark, 1988; Kimura and Ikeda, 1995, 1998; Kojima and Tomeoka, 1996; Krot et al., 1995, 1998, 2001, 2004; Weisberg and Prinz, 1998; Brearley, 1997; Choi et al., 2000; Zolotov et al., 2006; Brearley and Shearer, 2010; Ford and Brearley, 2008, 2010; Jogo et al., 2009, 2010). According to the asteroidal models (e.g., Krot et al., 1998a; Brearley 1997, 1999; Zolotov et al., 2006), CV chondrites experienced fluid-assisted thermal metamorphism under variable conditions (temperature and water/rock ratio) on the CV parent asteroid. This process resulted in mobilization of Ca, Si, Fe, Mg, Mn, Na, Cl, and S, the formation of a volatile-rich fluid and

replacement of primary phases in chondrules, CAIs and matrices by secondary minerals; some of the secondary minerals could have precipitated directly from a fluid. According to the nebular models (e.g., Palme and Wark, 1988; Kimura and Ikeda, 1995, 1998; Weisberg and Prinz, 1998), chondrules and refractory inclusions in oxidized Allende-like CV chondrites were exposed to a highly oxidizing nebular gas resulting in replacement of primary minerals by secondary minerals; matrix minerals (mainly ferroan olivine, ferroan high-Ca pyroxene, andradite, and nepheline) directly condensed from this nebular gas.

Here we describe the mineralogy, petrography, chemical and isotopic compositions of *Al3509* exposed in two polished thin sections, Mann#1 and Mann#2, and discuss the origin of this unique chondrule.

ANALYTICAL TECHNIQUES

Two polished thin sections, Mann#1 and Mann#2, were mapped in Mg, Ca, Al, Si, Na, Cl, Cr, and Ti K_{α} x-rays using a fully focused electron beam, 15 kV accelerating voltage, 100 nA beam current, 20 ms per pixel acquisition time, and resolution of ~ 5 μm per pixel with wavelength dispersive spectrometers on a Cameca SX-50 electron microprobe at the University of Hawai'i (UH). The elemental maps in Mg, Ca and Al K_{α} and Cl, Na, and Fe K_{α} were combined using an RGB-color scheme (Mg, Cl – red, Ca, Na – green, Al, Fe – blue) and ENVI (ENvironment for Visualizing Images, ITT Corporation) software package. The mineralogy of the chondrule was studied in backscattered electrons (BSE) using a JEOL JXA-8500F field-emission electron microprobe. Electron probe microanalyses were performed with the JEOL JXA-8500F microprobe using a 15 kV accelerating voltage, 15 nA beam current, beam size of 1 and 5 μm and wavelength dispersive x-ray spectroscopy. For each element, counting times on both peak and background were 30 sec. Matrix effects were corrected using PAP procedures.

Oxygen isotopic compositions were analyzed *in situ* with the UH Cameca ims-1280 ion microprobe using two analytical protocols. To measure O-isotope compositions of coarse ferroan high-Ca pyroxenes, a 2–3 nA focused Cs^+ primary ion beam was rastered over a 25×25 μm^2 area for 120–150 seconds. Then the raster was reduced to 10×10 μm^2 and data are collected for $4 \text{ sec} \times 40$ cycles. The secondary ion mass spectrometer was operated at -10 keV with a 50 eV energy window. $^{16}\text{O}^-$ was measured on a multicollector detector L'2, a Faraday cup with a 10^{10} ohm resistor; $^{18}\text{O}^-$ was measured on a Faraday collector H1 with a 10^{11} ohm resistor, and $^{17}\text{O}^-$ was

measured with the monocollector electron multiplier. To measure O-isotope compositions of fine-grained ($< 10 \mu\text{m}$) ferroan olivine, nepheline, and sodalite, a 30 pA focused Cs^+ primary ion beam was used. $^{16}\text{O}^-$ was measured on a multicollector detector L1, a Faraday cup with 10^{11} ohm resistor; $^{17}\text{O}^-$ was measured with the monocollector electron multiplier, and $^{18}\text{O}^-$ was measured with a multicollector electron multiplier H2. In both cases, the mass resolving power ($m/\Delta m$) for $^{16}\text{O}^-$ and $^{18}\text{O}^-$ was ~ 2000 , and that for $^{17}\text{O}^-$ was ~ 5500 , sufficient to separate interfering $^{16}\text{OH}^-$. A normal-incidence electron flood gun was used for charge compensation. Data were corrected for instrumental fractionation using San Carlos olivine, Cr-augite, and Miyakejima anorthite. To verify the positions of the sputtered region, the minerals studied for oxygen isotopes were photographed in secondary and backscattered electrons using the JEOL 5900LV scanning electron microscope or JEOL JXA-8500F microprobe before and after ion probe measurements.

Cl-S isotope measurements in sodalite were performed using the Lawrence Livermore National Laboratory Cameca NanoSIMS 50 using a primary Cs^+ beam of ~ 8 pA and diameter of ~ 200 nm. Depending upon the size of the sodalite grains, the primary beam was set to raster over areas between 8×8 and $30 \times 30 \mu\text{m}^2$. Because the collector configuration on the Cameca NanoSIMS 50 does not allow for simultaneous measurements of ^{35}Cl and ^{36}S without significantly distorting their respective peak shapes, measurements were performed in combined peak jumping, multi-collection mode, simultaneously measuring $^{28}\text{Si}^-$, $^{32}\text{S}^-$, $^{34}\text{S}^-$ and $^{36}\text{S}^-$, and subsequently stepping the magnetic field to measure $^{37}\text{Cl}^-$. A mass resolving power of ~ 3600 was used, sufficient to eliminate any contribution from $^{12}\text{C}_3^-$ or $^{35}\text{ClH}^-$ to the $^{36}\text{S}^-$ signal. However, this resolution was not high enough to resolve potential interferences from doubly-charged $^{35}\text{Cl}^{37}\text{Cl}^{2-}$ and $^{56}\text{Fe}^{16}\text{O}^{2-}$ species. To evaluate such effects, we analyzed terrestrial sodalite and wadalite. All the terrestrial samples yield $^{36}\text{S}/^{34}\text{S}$ ratios indistinguishable from normal, irrespective of the $^{35}\text{Cl}/^{34}\text{S}$ ratio, effectively ruling out any potential $^{35}\text{Cl}^{37}\text{Cl}^{2-}$ or $^{56}\text{Fe}^{16}\text{O}^{2-}$ interferences on $^{36}\text{S}^-$. We also carefully monitored and evaluated the potential interferences from $^{24}\text{Mg}^{48}\text{Ca}^{2-}$, $^{28}\text{Si}^{44}\text{Ca}^{2-}$, $^{40}\text{Ca}^{16}\text{O}_2^{2-}$ etc., and concluded that these are unlikely sources of error in our $^{36}\text{S}^-$ measurement. Due to the low intensity of $^{36}\text{S}^-$, the background at mass 36 was carefully evaluated; the mean background intensity for sodalite is ~ 0.013 cps. Data were processed as quantitative isotopic ratio images by using custom software (*L'image*; L.

Nittler) and were corrected for detector dead time and image shift from layer to layer. Regions of interest (ROIs) were defined based on elemental composition correlated with SEM images, and the isotopic composition for each ROI was calculated by averaging over the replicate layers.

Measured $^{37}\text{Cl}^-/^{34}\text{S}^-$ ion ratios were converted to atomic ratios using a relative sensitivity factor of 0.71 ± 0.04 for Cl/S, determined from measurements of terrestrial scapolite, $(\text{Na,Ca})_4(\text{Al}_3\text{Si}_9\text{O}_{24})\text{Cl}$. This relative sensitivity factor is similar to 0.69 reported by Nakashima et al. (2008), and the literature values for different minerals which are between 0.58 and 0.83 (Lin et al., 2005; Hsu et al., 2006; Ushikubo et al., 2007). Because ^{36}Cl decays by β -decay (98.1%) to ^{36}Ar and by electron capture and positron emission (1.9%) to ^{36}S , the $^{36}\text{Cl}/^{35}\text{Cl}$ ratios from the $^{36}\text{S}/^{34}\text{S}$ and $^{35}\text{Cl}/^{34}\text{S}$ measurements were calculated using a fraction of 0.019 of all ^{36}Cl decays going to ^{36}S .

The Al–Mg isotope measurements were performed using a modified ims-3f secondary ion mass spectrometer at the Lawrence Livermore National Laboratory following established procedures (e.g., Kennedy and Hutcheon, 1992; Goswami et al., 1994). The Al-rich phases were located by optical and ion imaging and a small field aperture inserted in the sample image plane to ensure acceptance of secondary ions for isotopic analysis only from a single phase of interest. Replicate measurements were performed in most cases. We also analyzed phases with low Al/Mg ratios (ferroan pyroxene) as well as appropriate terrestrial materials (e.g., Burma spinel, Dekalb diopside, San Carlos olivine, plagioclase and fassaite glass, and Lake County and Miakejima plagioclase) at the beginning and at the end of each measurement session.

Insofar as this study focused on the elucidation of the ^{26}Al – ^{26}Mg record, no special effort was made to characterize intrinsic mass-dependent fractionation in the chondrule and we do not report data for mass fractionation. The deviations in the measured $^{26}\text{Mg}/^{24}\text{Mg}$ ratios from the reference value, denoted by $\delta^{26}\text{Mg}$, were obtained by assuming a power-law mass-dependent fractionation corrections and using the relation:

$$\delta^{26}\text{Mg} = \Delta^{26}\text{Mg} - (\exp \{ \ln [(^{25}\text{Mg}/^{24}\text{Mg})_{\text{meas}} / (^{25}\text{Mg}/^{24}\text{Mg})_{\text{ref}}] / 0.514 \} - 1) \times 1000 \text{ [per mil]},$$

where

$$\Delta^i\text{Mg} = [\{ (^i\text{Mg}/^{24}\text{Mg})_{\text{meas}} / (^i\text{Mg}/^{24}\text{Mg})_{\text{ref}} \} - 1] \times 1000 \text{ [per mil]}; (i = 25, 26).$$

Reference values for $^{25}\text{Mg}/^{24}\text{Mg}$ and $^{26}\text{Mg}/^{24}\text{Mg}$ are 0.12663 and 0.13932, respectively (Catanzaro et al., 1966).

Two TEM samples of *Al3509* were prepared for study using the focused ion beam technique. A FEI Quanta 3D Field Emission Gun (FEG) SEM/Focus Ion Beam (FIB) instrument was used. These FIB sections sample a phase that could not be identified using SEM EDS or EPMA techniques. A platinum protective layer (2 μm thickness) was deposited in a strip across the area of interest prior to FIB sample preparation to minimize ion beam damage. The samples were removed from the thin section by the *in situ* lift out technique using an Omniprobe 200 micromanipulator and were transferred to a Cu TEM half grid. Final ion milling to electron transparency was carried out with the samples attached to the TEM grid.

The TEM studies were carried out using a JEOL 2010 HRTEM and a JEOL 2010F FEG TEM/STEM FASTEM instrument equipped with a GATAN GIF 2000 image filtering (GIF) system. HRTEM, electron diffraction and EDS X-ray analyses were carried out on the JEOL 2010 operating at 200 kV. X-ray analyses were obtained with an Oxford ISIS 200 EDS system using an Oxford Pentafet UTW EDS detector. The Cliff-Lorimer thin film approximation was used for quantification of EDS data using experimentally-determined k-factors. The JEOL 2010F was operated at 197 kV for energy filtered TEM (EFTEM), EFTEM spectral imaging (EFTEM-SI), electron energy loss spectroscopy (EELS), high angle annular dark field scanning TEM (HAADF-STEM) and HRTEM imaging.

RESULTS

MINERALOGY, PETROGRAPHY, AND CHEMICAL COMPOSITIONS

The *Al3509* is a large rounded object. The diameter of ~ 8 mm was reported by Mason and Taylor (1982). In two polished thin sections available for our study, Mann#1 and Mann#2, the diameters of the exposed regions of the object are 5 and 2.5 mm, respectively. X-ray elemental mapping revealed a core-mantle structure and a complex radial chemical zoning of the object (Figs. 1–4). Inspection of Figures 1a and b show the absence of any Mg-rich phases in the object. This is confirmed at much higher levels of magnification. Based on the chemical compositions, several zones or layers in the core (1–4) and the mantle (5–9) of *Al3509* can be identified; these zones/layers are indicated by numbers in Figures 1–5. In the polished section Mann#2, only four mantle layers, 6–9, are exposed. Defocused electron beam analyses of fine-grained zones are listed in Table 1. Electron microprobe analyses of nepheline, sodalite, ferroan olivine and high-

Ca pyroxene grains in the relatively coarse zones are listed in Table 2.

The object as a whole is Ca- and Al-rich; however, there are large variations in Ca and Al abundances between the core and the inner mantle (5, 6), and between the inner mantle and the outer (8, 9) mantle zones (Table 1; Figs. 1c,d). Although *Al3509* is apparently an igneous object, it shows widely variable textures that appear to represent different crystallization growth processes or sequences. *Al3509* contains none of the Al-rich or Mg-rich minerals commonly present in igneous (compact Type A, Type B, or Type C) CAIs or Al-rich chondrules such as melilite, spinel, Al,Ti-diopside, perovskite, plagioclase, forsterite, or magnesium-rich pyroxenes. Instead it consists entirely of fine-grained minerals (ferroan olivine, ferroan high-Ca pyroxene, nepheline, sodalite, and andradite). In Allende CAIs and chondrules, these minerals are considered to be the product of iron-alkali-halogen metasomatic alteration of primary high-temperature minerals (Krot et al., 1995, 1998a,b). Below we describe the mineralogy and petrography of compositionally distinct zones/layers in the core and the mantle of *Al3509*.

Core

Zone 1 constitutes the major portion of the core. It is rich in Ca, Na, and Cl (Table 1, Figs. 1c, 3c,d) and has a spherulitic texture (Fig. 5a–d). The spherulites are mineralogically-zoned and have a sodalite + high-Ca ferroan pyroxene central portion and a sodalite + ferroan olivine periphery (Figs. 5c,d).

Zone 2 is Cl-poor and has a lower Na content than zone 1 (Table 1, Fig. 3c,d). Calcium content is highly variable; Ca-rich and Ca-poor domains can be identified (Fig. 1c). The Ca-rich domains are composed of relatively coarse anhedral grains of ferroan Al-diopside intergrown with a very fine-grained Na-rich mineral (Figs. 5b, d) identified tentatively as nepheline using energy dispersive spectrometry (EDS). The Ca-poor domains are very fine-grained and consist of elongated crystals separated by a phase with a low mean atomic number (Fig. 7a). The defocused beam electron microprobe analyses of the Ca-poor domains have low totals (~ 85 wt%) due to high porosity and possibly the presence of hydrated minerals.

Zone 3 forms a thin layer around zone 2, has high Na and Cl contents, like zone 1, but lacks spherulitic textures and is Ca-poor (Table 1, Figs. 1c, 3c,d). It mainly consists of sodalite and ferroan olivine.

Zone 4 is represented by coarse elongated grains of ferroan Al-diopside (Table 2, Figs. 1,

5a,b). The central part of the pyroxene grains, indicated by arrows in Figure 5b, is partly filled by another mineral phase, which is too small for identification using EDS. The observations in transmitted polarized light suggest that the pyroxene grains crystallized away from the center and most likely represent remnants of veins crosscutting the core of *Al3509*. The presence of ferroan Al-diopside in nepheline-sodalite-bearing veins crosscutting the mantle of *Al3509* (Figs. 2c, 4a,f) supports this interpretation.

Mantle

The core is surrounded by a multilayered mantle (Figs. 1–5). The innermost layer 5, exposed only in section Mann#1, is thin and discontinuous (Figs. 1, 3) and consists of a very fine-grained material (Fig. 5e) that gives the low analytical totals (~89 wt%) of the defocused beam electron microprobe analyses (Table 1). This could be due to the high porosity of the fine-grained material and possibly to the presence of hydrated minerals.

Layer 6 is composed of compact regions of ferroan olivine-nepheline intergrowths and a fine-grained, porous interstitial material rich in Na and Al, possibly nepheline (Fig. 5e). The fine-grained material gives low analytical totals (~85 wt%) of electron microprobe analyses, most likely due to high porosity (Table 1).

The inner (5, 6) and outer (8, 9) mantle layers are separated by a thin discontinuous layer of andradite (zone 7; Fig. 5e) and crosscut by numerous veins composed of nepheline, sodalite, and ferroan Al-diopside (Figs. 3, 4).

Layer 8 consists of ferroan olivine, nepheline, sodalite, high-Ca pyroxene, and abundant rounded inclusions of a Fe,Mg,Al-silicate phase (Table 2). This phase described in the following section is commonly surrounded by a single layer of nepheline or a double layer of nepheline + unidentified phase having a needle-shaped morphology (Figs. 5e–g). Occasionally, the Fe,Mg,Al-phase contains needle-like inclusions of a Na-rich phase, possibly nepheline (Fig. 5f).

The outermost layer 9 consists of hopper and skeletal crystals of ferroan olivine intergrown with nepheline and sodalite, and minor high-Ca pyroxene (Table 2, Figs. 5g,h). In contrast, most CAIs in CV chondrites are surrounded by multilayered, refractory rims (Wark and Lovering, 1977). These Wark-Lovering rim layers are typically monomineralic and form a sequence (from inside to outside): spinel \pm hibonite \pm perovskite, melilite, Al-diopside, and forsterite. In the Allende-like oxidized CV chondrites, the Wark-Lovering rims show clear evidence of later

alteration as the spinel layer is enriched in FeO; the melilite layer is replaced by nepheline + sodalite + anorthite; and the forsterite rim is enriched in FeO and overgrown by a layer of hedenbergite \pm wollastonite \pm andradite. The Wark-Lovering rims do not have nepheline or sodalite as primary phases. No evidence of Wark-Lovering rim layers as defined above has been detected in any part of or within *Al3509*.

In addition to the mantle layers described above, Mann#2 contains a chemically and texturally distinct region in the outer mantle (Figs. 2, 4). This region is enriched in Si (Fig. 4b), depleted in Fe compared to the rest of the object, has a quenched, radial texture (Figs. 4c–e), and consists of skeletal crystals of sub-Ca pyroxene replaced to various degrees by ferroan high-Ca pyroxene, and interstitial sodalite. In the peripheral part of the region, these minerals are replaced by coarse ferroan olivine and sodalite (Fig. 4d).

TEM study of the unidentified Fe,Mg-Al-silicate phase

To seek an identification of the unidentified a Fe,Mg,Al-silicate phase referred to in the section on layer 8, it was characterized using TEM. The TEM observations were made on two FIB sections extracted from two separate grains of the unidentified Fe,Mg,Al-silicate phase. Each section cut across a region of a grain which contains inclusions of the needle phase shown in Figure 5f. Based on electron diffraction and EDS data, we have identified the unknown phase as ferroan olivine intergrown on a nanometer scale with an aluminous Fe-rich silicate phase. The TEM observations also confirm that the phase with a needle-shaped morphology is nepheline. Dark field STEM images showing the complex microstructure of the olivine in one of the FIB sections are shown in Figures 6a and b. This olivine is a composite grain consisting of three well-faceted subparallel elongate grains with low angle subgrains between them. The grains contain discontinuous lamellae of a second phase with lower Z contrast which typically occur at the subgrain boundaries between the three distinct grains. However, in some cases, the low Z lamellae occur within the subgrain itself, but do not appear to be coherently intergrown with the host. Some of these low Z lamellae also terminate in void space. This phase damages extremely rapidly under the electron beam, but is compositionally consistent with nepheline. It was not possible to obtain electron diffraction patterns from the nepheline due to a) the rapid beam damage and b) the fact that the nepheline appears to have suffered much more advanced ion beam damage during FIB sample preparation and hence was largely amorphous.

High resolution STEM imaging of the high Z phase shows that it is extremely heterogeneous at the nanometer-scale. Figure 6b shows that very thin lamellae of a higher Z-phase are coherently intergrown within the host phase. These lamellae have widths ranging from 1–2 nm and hence may represent single unit cells of a second phase. They are heterogeneously distributed and frequently show terminations within the host phase (Fig 6b). Figures 6d and e show a low magnification bright field TEM image and associated electron diffraction pattern from one of olivine grains from Figure 6a. The olivine grains show considerable evidence of internal strain, indicated by the complex mottled contrast in the image. This is confirmed in the electron diffraction pattern (Fig. 6b) which shows strong asterism in individual diffraction maxima, suggesting that although the grain is a single crystal, it consists of multiple, slightly misoriented subgrains. The strain in the olivine lattice may be the result of the presence of the interface dislocations between the olivine and the lamella phase, as well as subgrain boundary dislocations, such as those in the olivine grain shown in Figure 6e. Some grains have a notable strain-free zone, 0.1–0.2 microns in width at their outer edge (Figs. 6d,f).

In addition to evidence of significant strain, the olivines contain distinct nanometer-sized (10–100 nm) voids that are distributed heterogeneously through the grains (Figs. 6a,b,e,f). Most of the voids appear to be oriented with distinct internal facets parallel to the (100) plane of the olivine (e.g., Figs. 6a,b,e). The distribution of the voids is extremely variable, with some regions of the grains locally showing very high densities (e.g., Figs. 6a,e). The same crystals also contain regions of olivine that are completely free of voids (e.g., Fig. 6e).

X-ray analysis of the olivine host, high-Z lamellae and nepheline were carried out using STEM EDS techniques. The host olivine has a consistent composition of Fa_{38-40} , but each analysis almost invariably contains detectable, but variable concentrations of Al_2O_3 . The high-Z lamellae are too thin to determine their compositions precisely, but the data show that they are consistently enriched in Al_2O_3 relative to the host olivine phase (up to 22 wt% Al_2O_3). Given that the analyses must be mixtures of the host olivine and lamella phase, these data indicate that the lamella are extremely aluminous, an observation that is also consistent with the EPMA data (Table 2). Some lamellae are also enriched in Fe, but the data are quite variable with $\text{Fe}/(\text{Fe}+\text{Mg})$ ratios that overlap that of the host olivine ($\text{Fe}/(\text{Fe}+\text{Mg})=0.38-0.48$, c,f, olivine = $0.38-0.40$). Based on EDS analyses alone, it is not possible to identify the lamella phase unequivocally, because all the analyses are mixtures of two phases. However, the compositional data are

suggestive of a chlorite mineral, although this identification is not without problems. Assuming the phase is chlorite and calculating a mineral formula based on 28[O] atoms for the most aluminous analysis yields a mineral formula of $(\text{Mg}_{6.1}\text{Fe}_{4.7})\text{Al}_{1.8}(\text{Si}_{4.3}\text{Al}_{3.7})\text{O}_{20}(\text{OH})_8$. This composition would certainly be Si-deficient compared with most chlorite compositions which typically contain >5 Si cations per 28 [O]. The X-site sum (octahedral cations, Mg, Fe, Al) is also higher than the ideal 12 per formula unit. However, support for the identification of this phase as chlorite comes from electron diffraction data from regions of the olivine grains that contain a high density of lamellae. Figure 7 shows an [011] zone axis pattern for an olivine grain which contains distinct extra reflections parallel to the [100] direction of the olivine. These reflections are of weaker intensity than the host olivine and are more diffuse. The electron diffraction pattern for the intergrown phase is clearly a zone axis pattern and shows that it has a well-constrained crystallographic orientation relationship with the host olivine, i.e. the two phases are coherently intergrown. The calculated *d*-spacing of the intergrown phase parallel to the [100] direction of the olivine, based on these diffraction maxima is ~ 1.42 nm, consistent with the (001) basal spacing of chlorite. However, although the diffraction pattern is clearly a zone axis, the *d*-spacings and angular relationships between the diffraction vectors are not an exact match for chlorite, although they are close. This discrepancy could be the result of several factors including the fact that the lattice parameters for the intergrown phase may be significantly distorted due to misfit strain with the olivine, particularly so because the lamellae are only one to two unit cells in thickness. In addition, the highly aluminous composition of the phase may result in a marked change in the lattice parameters compared with the clinocllore unit cell used to calculate the theoretical diffraction data. Based on the compositional and crystallographic data, it therefore seems most probable that this phase is a highly aluminous chlorite. The deficiency in Si in the tetrahedral sites may be a reflection of the fact that the chlorite formed in a highly ultramafic bulk composition (Si-undersaturated), unlike typical terrestrial environments in which chlorite is a stable phase. We consider the identification of chlorite as a reasonable inference, but not a definitive one.

Fine-grained rim

The object is surrounded by a fine-grained rim composed of ferroan olivine, nepheline, and sodalite (Fig. 8). The rim is depleted in Ca relative to the neighboring matrix. Abundant nodules of Ca,Fe-rich pyroxenes are observed at boundary between the rim and the matrix.

In all of the zones described above and in the veins, there is **no** major change in the overall mineralogy, and, hence, no direct evidence of late stage alteration producing a distinctive mineral assemblages except for very minor possibly hydrous phases.

ISOTOPIC COMPOSITIONS

Oxygen isotopes

Oxygen isotopes were measured in coarse ferroan Al-diopside grains (veins) in the core of *Al3509* (Fig. 9a), in the Fe,Mg,Al-silicate phase in the mantle layer 8 (Fig. 9b, EA1), and in nepheline and sodalite veins crosscutting the mantle (Figs. 9c,d, EA1). To check whether the *Al3509* minerals contain any significant amount of structural water, the $^{16}\text{OH}^-$ count rate in each of the grains analyzed was measured after O-isotope measurements. The $^{16}\text{OH}^-$ count rates in nepheline, sodalite, ferroan olivine, and the unidentified phase were similarly low ($\sim 10^4$ c/s) and not distinguishable from the background. In Figure 10, the oxygen isotopic compositions of these grains are plotted together with the compositions of the secondary Ca,Fe-rich pyroxenes and sodalite in the Allende matrix, Allende dark inclusions (Krot et al., 2000) and a rim around the Allende Type B CAI *TS24* (Cosarinsky et al., 2003). Oxygen isotopic compositions of all these minerals plot along a mass-dependent fractionation line at a $\Delta^{17}\text{O}$ value of $\sim -2.5 \pm 0.5\text{‰}$ (Fig. 10).

^{26}Al - ^{26}Mg systematics

The Al-Mg isotopic results (2σ error bars) for sodalite and ferroan pyroxene are shown in Figure 11. It is evident that there is no evidence for any enrichment in ^{26}Mg even in sodalite with extremely high Al/Mg ratios. The pyroxene $^{26}\text{Mg}/^{24}\text{Mg}$ ratio is indistinguishable from the terrestrial value. The upper limit of the inferred initial $^{26}\text{Al}/^{27}\text{Al}$ ratio in *Al3509* is 3×10^{-6} . This is in accord with the upper bounds found for sodalite samples in alteration products of CAIs (e.g., Lin et al., 2005; Hsu et al., 2006; Ushikubo et al., 2007). Relative to the canonical $^{26}\text{Al}/^{27}\text{Al}$ ratio of $\sim 5 \times 10^{-5}$, the low value of $(^{26}\text{Al}/^{27}\text{Al})_0$ reported here would require a time interval for formation of ~ 3 Myr following the crystallization of Type B CAIs.

^{36}Cl - ^{36}S systematics

The Cl-S isotopic results for sodalite are plotted in Figure 12. Two features are immediately apparent. First, all of the *Al3509* sodalite grains measured show large excesses of ^{36}S , up to 1.7 times the normal value. Second, the data show no evidence for a correlation between the magnitude of excess ^{36}S and the $^{35}\text{Cl}/^{34}\text{S}$ ratio; the sodalite with the highest $^{36}\text{S}/^{34}\text{S}$ ratio has the third lowest $^{35}\text{Cl}/^{34}\text{S}$ ratio ($^{35}\text{Cl}/^{34}\text{Cl} = 4851$). Thus, we have no *prima facie* evidence for *in situ* decay of ^{36}Cl . However, the $^{36}\text{S}/^{34}\text{S}$ ratios of sodalite in *Al3509* show large enrichments in ^{36}S , strongly suggesting that the sodalite formed in an environment where ^{36}Cl had once been present. Whether the ^{36}Cl had decayed prior to sodalite formation or was incorporated live into the sodalite and subjected to later redistribution remains unclear. The lack of any correlation between the $^{36}\text{S}/^{34}\text{S}$ and $^{35}\text{Cl}/^{34}\text{S}$ ratios in *Al3509* coupled with the extensive evidence for multiple stages of crystallization and recrystallization preclude using these data to estimate the initial abundance of ^{36}Cl . Our preferred interpretation is that abundant ^{36}Cl had been present in this object and that radiogenic ^{36}S was redistributed during the subsequent recrystallization processes.

DISCUSSION

The spherical shape of *Al3509*, its locally preserved igneous, quenched texture (Figs. 5b–d), and the high Ca and Al and low Ti contents show that the object is a Ca,Al-rich chondrule. The lack of minerals commonly observed in igneous CAIs (spinel, Al,Ti-diopside, melilite, anorthite, perovskite), and the lack of the Wark-Lovering rim layers all indicate that the object is not a CAI. In contrast to the typical CV carbonaceous chondrite Ca,Al-rich chondrules having porphyritic textures (e.g., Srinivasan et al., 1999; Krot et al., 2002) and magnesium-rich, alkali-poor compositions of phenocrysts (spinel, Al,Ti-diopside, anorthite, forsteritic olivine, and Mg-rich pyroxenes), *Al3509* has a non-porphyritic texture and is very volatile-rich. It consists almost entirely of fine-grained ferroan olivine, ferroan Ca, Al-rich pyroxene, nepheline, sodalite, andradite, and a rare Fe,MgAl-silicate phase which may be chlorite. These observations and some of the textures indicate that either *Al3509* rapidly crystallized from a melt rich in Na, Cl, and Fe or it experienced postcrystallization open-system alteration and most of the volatile elements were introduced into the object during this alteration. The complete absence of spinel, perovskite or any of the major phases characteristic of CAIs indicates that the chondrule is not plausibly a replacement of a pre-existing CAI. In particular, phases such as spinel, perovskite

and Al,Ti-diopside are resistant to alteration and some of them should be preserved through extensive alteration and metamorphism. We infer that *Al3509* is a unique Ca,Al-rich chondrule; it is not a CAI nor a replacement product of a pre-existing CAI.

In contrast to the typical Ca,Al-rich chondrules in CV chondrites having porphyritic textures and magnesium-rich, alkali-poor phenocryst compositions (Srinivasan et al., 1999; Krot et al., 2002), Ca, Al-rich chondrules dominantly composed of glass have been found in unequilibrated ordinary chondrites but not in CV chondrites (Bischoff and Keil, 1984; Krot and Rubin, 1994; Russell et al., 1996, Nehru et al., 2008). These glassy chondrules contain some porphyritic crystals or show development of devitrification with incipient crystals. Glassy chondrules rich in Na are exceptionally rare. The rare examples are Cl-free and always contain either phenocrysts and/or xenocrysts of Mg-rich minerals (olivine, pyroxene, and/or spinel). Two such chondrules have been shown to contain evidence for the presence of ^{26}Al ($^{26}\text{Al}/^{27}\text{Al} \sim 10^{-5}$; Russell et al., 1996). While *Al3509* shows some evidence that it formed from a molten droplet, it does not have any other chemical affinity with Na-rich glass chondrules. Nonetheless, the existence of Na-rich glass chondrules shows that late formation of liquid silicate droplets rich in the highly volatile element Na occurred. Due to the high vapor pressure of Na, none of these Na-rich glass chondrules could have formed under low nebular pressures at the high temperatures required for melting.

A possible connection between *Al3509* and typical (ferromagnesian and Al-rich) chondrules and refractory inclusions in the Allende meteorite is found in the fact that the mineralogy of *Al3509*, particularly the presence of sodalite and nepheline, is extremely close to that found in the late-stage alteration products of the Allende CAIs and chondrules (Ikeda and Kimura, 1995; Kimura and Ikeda, 1995, 1998; Krot et al., 2002, 2007, 2010). The nature of the metamorphic process that impregnated the Allende CAIs and chondrules with such very volatile components is poorly understood. This event must have occurred in some type of planetary environment prior to the incorporation of the CAIs and chondrules into the Allende parent body. This environment could be either a “proto-Allende” or another body/bodies from which Allende subsequently formed or was assembled. The presence of extensively metasomatically altered chondritic lithic clasts (dark inclusions) in the Allende meteorite supports this conclusion (e.g., Fruland et al., 1987; Kurat et al., 1989; Johnson et al., 1990; Buchanan et al., 1997; Krot et al., 2001; Pravdivtseva et al., 2003). This alteration must have taken place in a much higher density

environment than is possible under nebular conditions. The interior of a planetary body or a shock event resulting from a collision between meteorite parent bodies/proto-asteroids are two plausible scenarios.

The nature of the fluid causing the alteration of the *Al3509* precursor is not known. One possibility is that *Al3509* represents the bulk fluid and the observed alteration of CAIs and typical chondrules reflects circulation of that fluid throughout the proto-Allende body. The rare occurrences of hydrous minerals in *Al3509* argue against a high abundance of H₂O in the fluid. This is in accord with the results of Brearley (1997, 1999), who found evidence of modest aqueous alteration but no evidence of a pervasive H₂O-dominated alteration in CAIs or ferromagnesian chondrules in Allende.

Alternatively, the bulk composition of *Al3509* may not represent the composition of the fluid and a more mobile component is required. There has been no report of fluid inclusions in CV meteorites, but evidence for the presence of Na- and Cl-rich volatiles and fluid inclusions with water as the principal fluid phase has been found in H6 chondrites in the form of halite crystals (Zolensky et al., 1999). A careful investigation of this halite showed that it had a ⁴⁰Ar/³⁹Ar age of 4.5 Gyr and contained essentially pure ¹²⁹Xe from decay of ¹²⁹I with the inferred initial ¹²⁹I/¹²⁷I ratio of 1.3×10^{-4} (Whitby et al., 2000). Thus, the formation and transport of a Na- and Cl-rich fluid must have occurred in protoplanetary bodies during relatively early epochs. Nakashima et al. (2010) showed that a halite grain from the Zag meteorite contained no ³⁶S excess (³⁶Cl/³⁵Cl < 3.2×10^{-7}). For the case of the Zag halite, the formation and transport of Na- and Cl-rich fluid must have occurred during relatively early epochs but after any initial ³⁶Cl had decayed. In the case of *Al3509*, there is a clear indication that excess ³⁶S from decay of ³⁶Cl was present but must have been subject to recrystallization and redistribution. While ³⁶Ar has not been studied in this object, all previous studies indicate that ³⁶Ar would only be present at very low levels corresponding to ³⁶Cl/³⁷Cl of $\sim 10^{-8}$ (Villa et al., 1981; Gobel et al., 1982). It appears that this dilemma may be resolved from the work of Turner et al. (2009) who showed that Ar can be effectively lost relative to Xe during heating due to lower activation energy for Ar diffusion. Release of essentially all of the Cl-correlated Ar and retention of the I-correlated Xe on a timescale of 1 Myr would require sustained temperatures of approximately 460°C and 740°C, respectively. This interpretation would then require that all such samples had undergone a post formation heating event. If we assume no radiogenic ³⁶Ar in *Al3509*, then, the presence of large

excesses of radiogenic $^{129}\text{Xe}^*$ require similar post-formation heating. This model is in consonance with the isotopic and textural observations presented above.

A distinct problem arises with regard to ^{36}Cl . The source of the ^{36}Cl has been attributed to energetic particle irradiation by an active early Sun as no stellar source appears possible (Wasserburg et al., 2006). However, the results of irradiation models do not appear to yield the abundances of short lived nuclei observed (e.g., Leya et al., 2003; Duprat and Tatischeff, 2007). If ^{36}Cl is from an episode of energetic particle bombardment of either distributed dust or an extended solid target of approximately solar (CI) composition, there should be some signatures of other nuclear reaction products, particularly for the observed levels of $^{36}\text{Cl}/^{37}\text{Cl}$ (4×10^{-6} to 2×10^{-5}). Such an irradiation would concurrently result in major production of several short-lived nuclei, including ^7Be , ^{10}Be , ^{26}Al , ^{36}Cl , ^{41}Ca , and ^{53}Mn . However, from the currently available data (e.g., Lin et al., 2005; Hsu et al., 2006; Ushikubo et al., 2007; Nakashima et al., 2008; Jacobsen et al., 2009), there is no evidence for ^{26}Al correlated with the ^{36}S excesses. A possible solution to this problem may be that a target material was ice highly enriched in Cl with a very little silicate dust component, which could yield high ^{36}Cl , ^7Be , and ^{10}Be without major contributions to heavier short-lived radionuclides. A search for associated nuclear effects should be made in samples with ^{36}Cl .

The source of the extremely high Cl and Na contents in *Al3509* is also a challenging issue. Assuming that ^{26}Al is the dominant heat source at $^{26}\text{Al}/^{27}\text{Al} = 5 \times 10^{-5}$, parent bodies of radius greater than a few hundred meters will be heated sufficiently in their interiors to drive volatile elements to the exterior regions (Lee et al., 1977). It should thus be possible to locally obtain large enrichments of many volatile elements which would have to be further concentrated to precipitate the Na-, Cl-rich phases found in *Al3509*. We would expect H_2O , which is an abundant nebular gas and which would be present in any very early formed hydrous phases, to be the major volatile component. However, there is no evidence for significant aqueous alteration of *Al3509*. It may therefore necessary to consider that either CO_2 or some other compound might be the mobile component or that the bulk chemical composition of *Al3509* is the full metasomatizing agent. The possibility that CO_2 is a significant component in the metamorphic processes affecting meteorites has received relatively little attention as it is not a compound associated with nebular conditions. Calcite has been found in many carbonaceous chondrites (Brearley and Jones, 1989) and it has been found surrounding a vuggy hibonite mass (with

$^{26}\text{Al}/^{27}\text{Al} = 5 \times 10^{-5}$) in the Blue Angel CAI from Murchison (Armstrong et al., 1982). However, we note that the solubility of Na and Cl in CO_2 is negligible at pressures of up to 70 mpa (Zakirov et al., 2007).

We suggest that *Al3509* may possibly represent the bulk fluid with very little water activity, but as indicated above, we cannot infer any further properties of the fluids involved. A study of the phase equilibria for a system with the bulk composition of *Al3509* (with and without H_2O) would be very important in clarifying the matter. It is well known that sodalite, can be produced under hydrothermal conditions. The issue at hand is whether the assemblage of minerals reported here are mutually compatible with growth from an aqueous medium without causing more extensive aqueous alteration to these phases or of the host phases in CAIs.

ACKNOWLEDGMENTS

This work was supported by NASA Grants NAG5-10610 and NNX07AI81G (A.N. Krot, P.I.), NAG5-4212 (K. Keil, P.I.), NNG06GG37G (A.J. Brearley, P.I.) and NNH04AB47I (I.D. Hutcheon, P.I.) and by the Glenn Seaborg Institute. This work was performed under the auspices of the U.S. Department of Energy by Lawrence Livermore National Laboratory under Contract DE-AC52-07NA27344. This is Hawaii Institute of Geophysics and Planetology Publication No. xxx and School of Ocean and Earth Science and Technology Publication No. xxx. G. J. Wasserburg acknowledges support by a NASA Cosmochemistry RTOP to J. Nuth, at GSFC, and by the Epsilon Foundation.

REFERENCES

- Alexander C. M. O'D., Barber D. J., and Hutchison R. (1989) The microstructure of Semarkona and Bishunpur. *Geochim. Cosmochim. Acta*, **53**, 3045–3057.
- Armstrong J. T., Meeker G. P., Huneke J. C., and Wasserburg G. J. (1982) The Blue Angel. I - The mineralogy and petrogenesis of a hibonite inclusion from the Murchison meteorite. *Geochim. Cosmochim. Acta*, **46**, 575–595.
- Bischoff A. and Keil K. (1984) Al-rich objects in ordinary chondrites – Related origin of carbonaceous and ordinary chondrites and their constituents. *Geochim. Cosmochim. Acta*, **48**, 693–709.

- Brearley A. J. (1997) Disordered biopyriboles, amphibole, and talc in the Allende meteorite; products of nebular or parent body aqueous alteration? *Science*, **276**, 1103–1105.
- Brearley A. J. (1999) Origin of graphitic carbon and pentlandite in matrix olivines in the Allende meteorite. *Science*, **285**, 1380–1382.
- Brearley A. J. (2005) The action of water. In *Meteorites and the Early Solar System II* (eds. Lauretta D. S., Leshin L. A., and McSween H. Y. Jr.), Univ. of Arizona, Tucson.
- Brearley A. J. and Jones R. H. (1998) In *Planetary Materials, Rev. Mineral.*, **36**, 1–398, Mineral. Soc. Am., Washington, DC.
- Brearley A. J. and Shearer C. K. (2000) Origin of calcium-iron-rich pyroxenes in Allende matrix: Clues from rare-earth-element abundances (abstract). *Meteorit. Planet. Sci.*, **35** (Suppl.), A33.
- Bridges J. C., Alexander C. M. O'D., Hutchison R., Franchi I. A., and Pillinger C. T. (1997) Sodium-, chlorine-rich mesostases in Chainpur (LL3) and Parnallee (LL3) chondrules. *Meteorit. Planet. Sci.*, **32**, 555–565.
- Buchanan P. C., Zolensky M. E., and Reid A. M. (1997) Petrology of Allende dark inclusions. *Geochim. Cosmochim. Acta*, **61**, 1733–1743.
- Catanzaro E. J., Murphy T. J., Garner, E. L. and Shields W. R. (1966) Absolute isotopic abundance ratios and atomic weights of magnesium. *J. Res. Natl. Bur. Stand.* **70a**, 453–458.
- Choi B.-G., Krot A. N., and Wasson J. T. (2000) Oxygen-isotopes in magnetite and fayalite in CV chondrites Kaba and Mokoia. *Meteorit. Planet. Sci.*, **35**, 1239–1249.
- Clarke R. S., Jarosewich E., Jr., Mason B., Nelen J., Gomez M., and Hyde J. R. (1970) The Allende, Mexico, meteorite shower. *Smithsonian Contrib. Earth Sci.*, **5**, 1–53.
- Duprat J. And Tatischeff V. (2007) Energetic constraints on in situ production of short lived nuclei in the early solar system. *Astrophys. J.*, **671**, 169–172.
- Ford R. L. and Brearley A. J. (2008) Element exchange between matrix and CAIs in the Allende meteorite (abstract). *Lunar Planet. Sci.*, **39**, #2399.
- Ford R. L. and Brearley A. J. (2010) Discovery of vesuvianite and kaolinite formed during the alteration of melilite in an Allende Type A CAI: Characterization by FIB/TEM (abstract). *Lunar Planet. Sci.*, **41**, #1402.
- Fruland R. M., King A. E., and McKay D. S. (1978) Allende dark inclusions. In *Proc. Lunar Sci. Conf. 9th*, 1305–1329.

- Gobel R., Begemann F., and Ott U. (1982) On neutron-induced and other noble gases in Allende inclusions. *Geochim. Cosmochim. Acta*, **46**, 1777–1792.
- Goswami J. N., Srinivasan G., and Ulyanov A. A. (1994) Ion microprobe studies of Efremovka CAIs: I. Magnesium isotope composition. *Geochim. Cosmochim. Acta*, **58**, 431–447.
- Johnson C. A., Prinz M., Weisberg M. K., Clayton R. N., and Mayeda T. K. (1990) Dark inclusions in Allende, Leoville, and Vigarano: Evidence for nebular oxidation of CV3 constituents. *Geochim. Cosmochim. Acta*, **54**, 819–831.
- Hewins R. H. (1997) Chondrules. *Ann. Rev. Earth Planet. Sci.*, **25**, 61–83.
- Hsu W., Guan Y., Leshin L. A., Ushikubo T., and Wasserburg G. J. (2006) A late episode of irradiation in the early solar system: Evidence from extinct ^{36}Cl and ^{26}Al in meteorites. *Astrophys. J.*, **640**, 525–529.
- Ikeda Y. and Kimura M. (1995) Anhydrous alteration of Allende chondrules in the solar nebula I: Description and alteration of chondrules with known oxygen-isotopic compositions. *Proc. NIPR Symp. Antarct. Meteorites*, **8**, 97–122.
- Ishii H. A., Krot A. N., Bradley J. P., Keil K., Nagashima K., Teslich N., Jacobsen B., Yin Q.-Z. (2010) Discovery, mineral paragenesis and origin of wadalite in a meteorite. *Amer. Mineral.*, **95**, 440–448.
- Jacobsen B., Matzel J., Hutcheon I. D., Ramon E., Krot A. N., Ishii H., Nagashima K., and Yin Q.-Z. (2009) The ^{36}Cl - ^{36}S systematic of CAI wadalite from the Allende meteorite: evidence for possible early incorporation of live ^{36}Cl into CAIs (abstract). *Lunar Planet. Sci.*, **40**, #2553.
- Jogo K., Nakamura T., Noguchi T., and Zolotov M. Yu. (2009) Fayalite in the Vigarano CV3 carbonaceous chondrite: Occurrences, formation age and conditions. *Earth Planet. Sci. Lett.*, **287**, 320–328.
- Jogo K., Nakamura T., Ito M., and Messenger S. (2010) Mn-Cr systematics of secondary fayalites in the CV3 carbonaceous chondrites A 881317, MET 00430 and MET 01074 (abstract). *Lunar Planet. Sci.*, **41**, #1573.
- Kennedy A. K. and Hutcheon I. D. (1994) Chemical and isotopic constraints on the formation and crystallization of SA-1, a basaltic Allende plagioclase-olivine inclusion. *Meteoritics*, **27**, 539–554.

- Kimura M. and Ikeda Y. (1995) Anhydrous alteration of Allende chondrules in the solar nebula; II, Alkali-Ca exchange reactions and formation of nepheline, sodalite and Ca-rich phases in chondrules. *Proc. NIPR Symp. Antarctic Meteorites*, **8**, 123–138.
- Kimura M. and Ikeda Y. (1998) Hydrous and anhydrous alterations of chondrules in Kaba and Mokoia CV chondrites. *Meteorit. Planet. Sci.*, **33**, 1139–1146.
- Krot A. N. and Rubin A. E. (1994) Glass-rich chondrules in ordinary chondrites. *Meteoritics* **29**, 697–707.
- Krot A. N., Scott E. R. D., and Zolensky M. E. (1995) Mineralogic and chemical variations among CV3 chondrites and their components: Nebular and asteroidal processing. *Meteoritics*, **30**, 748–775.
- Krot A. N., Petaev M. I., Scott E. R. D., Choi B.-G., Zolensky M. E., and Keil K. (1998a) Progressive alteration in CV3 chondrites: More evidence for asteroidal alteration. *Meteorit. Planet. Sci.*, **33**, 1065–1085.
- Krot A. N., Zolensky M. E., Keil K., Scott E. R. D., and Nakamura K. (1998b) Secondary Ca-Fe-rich minerals in the Bali-like and Allende-like oxidized CV3 chondrites and Allende dark inclusions. *Meteorit. Planet. Sci.*, **33**, 623–645.
- Krot A. N., Hiyagon H., Petaev M. I., and Meibom A. (2000) Oxygen isotopic compositions of secondary Ca-Fe-rich silicates from the Allende dark inclusions: Evidence against high-temperature formation (abstract). *Lunar Planet. Sci.* **31**, #1463.
- Krot A. N., Petaev M. I., Meibom A., and Keil K. (2001) *In situ* growth of Ca-rich rims around Allende dark inclusions. *Geochem. International*, **36**, 351–368.
- Krot A. N., Hutcheon I. D., and Keil K. (2002) Anorthite-rich chondrules in the reduced CV chondrites: evidence for complex formation history and genetic links between CAIs and ferromagnesian chondrules. *Meteorit. Planet. Sci.*, **37**, 155–182.
- Krot A. N., Petaev M. I., and Bland P. A. (2004) Multiple formation mechanisms of ferrous olivine in CV3 carbonaceous chondrites during fluid-assisted metamorphism. *Antarctic Meteorite Res.*, **17**, 154–172.
- Krot A. N., Amelin Y., Cassen P., and Meibom A. (2005) Young chondrules in CB chondrites from a giant impact in the early Solar System. *Nature*, **436**, 989–992.

- Krot A. N., Yurimoto H., Hutcheon I. D., Libourel G., Chaussidon M., Petaev M. I., MacPherson G. J., Paque-Heather J., and Wark. D. (2007) Anorthite-rich, igneous (Type C) Ca,Al-rich inclusions from the CV carbonaceous chondrite Allende: Evidence for multistage formation history. *Geochim. Cosmochim. Acta*, **71**, 4342–4364.
- Krot A. N., Nagashima K., Hutcheon I. D., Ishii H. A., Jacobsen B., Yin Q.-Z., Davis A. M., and Simon S. B. (2010) Mineralogy, petrography, oxygen and magnesium isotopic compositions and formation age of grossular-bearing assemblages in the Allende CAIs (abstract). *Lunar Planet. Sci.*, **41**, #1441.
- Kurat G., Palme H., Brandstätter F. and Huth J. (1989) Allende xenolith AF: Undisturbed record of condensation and aggregation of matter in the solar nebula. *Zeitschr. Naturforsch.*, **44a**, 988–1004.
- Lee T., Papanastassiou D. A., and Wasserburg G. J. (1977) Aluminum-26 in the early solar system: fossil or fuel. *Astrophys. J.*, **211**, L107–L110.
- Leya I., Halliday A. N., and Wieler R. (2003) Predictable consequences of nucleosynthesis by spallation reactions in the early solar system. *Astrophys. J.*, **594**, 605–616.
- Lin Y., Guan Y., Leshin L. A., Ouyang Z., and Wang D. (2005) Short-lived chlorine-36 in a Ca- and Al-rich inclusion from the Ningqiang carbonaceous chondrite. *Proc. Nat. Acad. Sci.*, **102**, 1306–1311.
- Mason B. and Martin P. M. (1977) Geochemical differences among components of Allende meteorite. *Smithson. Contrib. Earth Sci.*, **19**, 84–95.
- Mason B. and Taylor S. R. (1982) Inclusions in the Allende meteorite. *Smithsonian Contrib. Earth Sci.*, **25**, pp. 1–30.
- Matzel J. E. P., Jacobsen B., Hutcheon I. D., Krot A. N., Nagashima K., Yin Q.-Z., Ramon E. C., Weber P. K., and Wasserburg G. J. (2010) Distribution and origin of ^{36}Cl in Allende CAIs (abstract). *Lunar Planet Sci.*, **41**, #2631.
- Nakashima D., Ott U., Hoppe P., and El Goresy A. (2008) Search for extinct ^{36}Cl : Vigarano CAIs, the Pink Angel from Allende, and a Ningqiang chondrule. *Geochim. Cosmochim. Acta*, **72**, 6141–6153.
- Nakashima D., Ott U., and Hoppe P. (2010) Search for extinct chlorine-36: a halite grain from the Zag meteorite (abstract). *Meteorit. Planet. Sci.*, **45**, #5289.

- Nehru C. E., Weisberg M. K., Ebel D. S., Boesenberg J. S., and Connolly H. C., Jr. (2008) Origin of Na-, Al-, glass-rich chondrules in H, L and LL chondrites (abstract). *Lunar Planet. Sci.*, **39**, #1697.
- Palme H. and Wark D. A. (1988) CV-chondrites: High temperature gas-solid equilibrium vs. parent body metamorphism (abstract). *Lunar Planet. Sci.*, **19**, 879–880.
- Pravdivtseva O. V., Krot A. N., Hohenberg C. M., Meshik A. M., Weisberg M. K., and Keil K. (2003) The I-Xe record of alteration in the Allende CV chondrite. *Geochim. Cosmochim. Acta*, **67**, 5011–5026.
- Russell S. S., Srinivasan G., Huss G. R., Wasserburg G. J., and MacPherson G. J. (1996) Evidence for widespread ^{26}Al in the solar nebula and constraints for nebula time scales. *Science*, **273**, 757–762.
- Srinivasan G., Huss G. R. and Wasserburg G. J. (1999) A petrographic, chemical, and isotopic study of calcium-aluminum-rich inclusions and aluminum-rich chondrules from the Axtell (CV3) chondrite. *Meteorit. Planet. Sci.*, **35**, 1333–1354.
- Turner G., Crowther S. A., Burgess R., Wasserburg G. J., Kelley S. P., and Gilmour J. D. (2009) Pink Angel: Argon and xenon diffusion, I-Xe chronology and the ^{36}Cl problem (abstract). *Meteorit. Planet. Sci.*, **44**, #5255.
- Ushikubo T., Guan Y., Hiyagon H., Sugiura N., and Leshin L. A. (2007) ^{36}Cl , ^{26}Al , and O isotopes in an Allende type B2 CAI: Implications for multiple secondary alteration events in the early solar system. *Meteorit. Planet. Sci.*, **42**, 1267–1279.
- Villa I. M., Huneke J. C., Papanastassiou D. A., and Wasserburg G. J. (1981) The Allende Pink Angel: Chronological constraints from Xe, Ar, and Mg (abstract). *Lunar Planet. Sci.*, **12**, 1115–1117.
- Wark D. A. and Lovering J. F. (1977) Marker events in the early solar system: Evidence from rims on Ca-Al-rich inclusions in carbonaceous chondrites. *Proc. Lunar Sci. Conf.*, **8**, 95–112.
- Wasserburg G. J. (1985) Short lived nuclei in the early solar system. In *Protostars and Planets II*, Univ. Arizona Press, pp.703–737.
- Wasserburg G. J. and Huneke J. C. (1979) I-Xe dating of I-bearing phases in Allende (abstract). *Lunar Planet. Sci.* **10**, 1307–1309.
- Wasserburg G. J., Busso M., Galino R., and Nollett K. M. (2006) Short-lived nuclei in the early Solar System: Possible AGB sources. *Nuclear Physics A*, **777**, 5–69.

- Weisberg M. K. and Prinz M. (1998) Fayalitic olivine in CV3 chondrite matrix and dark inclusions: A nebular origin. *Meteorit. Planet. Sci.*, **33**, 1087–1111.
- Whitby J., Burgess R., Turner G., Gilmour J., and Bridges J. (2000) Extinct ^{129}I in halite from a primitive meteorite: Evidence for evaporite formation in the early solar system. *Science*, **288**, 1819–1821.
- Zakirov I. V., Sretenskaja N. G., Aranovich L. Y., and Volchenkova V. A. (2007) Solubility of NaCl in CO₂ at high pressure and temperature: First experimental measurements. *Geochim. Cosmochim. Acta*, **71**, 4251–4255.
- Zolotov M. Yu., Mironenko M. V., and Shock E. L. (2006) Thermodynamic constraints on fayalite formation on parent bodies of chondrites. *Meteorit. Planet. Sci.*, **41**, 1775–1796.
- Zolotov M. Yu. and Mironenko M. V. (2007) Hydrogen chloride as a source of acid fluids in parent bodies of chondrites (abstract). *Lunar Planet. Sci.*, **38**, #2340.

Table 1. Average defocused beam analyses of fine-grained core and mantle zones in the *Al3509* chondrule.

zones	no an.	SiO ₂	TiO ₂	Al ₂ O ₃	Cr ₂ O ₃	FeO	MnO	MgO	CaO	Na ₂ O	K ₂ O	Cl	total
1, core	11	45.1	0.06	13.6	0.14	5.6	0.08	9.0	14.2	7.7	0.19	2.4	98.1
		<i>0.5</i>	<i>0.02</i>	<i>0.6</i>	<i>0.02</i>	<i>0.9</i>	<i>0.03</i>	<i>1.1</i>	<i>0.8</i>	<i>0.6</i>	<i>0.2</i>	<i>0.2</i>	<i>0.8</i>
1, rim	5	36.1	0.06	27.0	0.16	4.9	0.05	7.9	0.20	17.6	0.02	5.2	99.2
		<i>0.3</i>	<i>0.02</i>	<i>1.4</i>	<i>0.02</i>	<i>1.2</i>	<i>0.02</i>	<i>2.0</i>	<i>0.06</i>	<i>1.6</i>	<i>0.01</i>	<i>0.40</i>	<i>1.0</i>
3	10	34.7	0.09	17.3	0.20	8.8	0.09	13.8	0.82	8.4	0.95	0.12	85.2
		<i>1.3</i>	<i>0.02</i>	<i>0.9</i>	<i>0.02</i>	<i>0.5</i>	<i>0.02</i>	<i>1.2</i>	<i>0.34</i>	<i>0.4</i>	<i>0.05</i>	<i>0.05</i>	<i>2.9</i>
5	8	45.3	0.10	17.8	0.20	2.0	0.01	10.2	8.4	3.9	1.0	0.12	89.0
		<i>1.1</i>	<i>0.02</i>	<i>1.0</i>	<i>0.02</i>	<i>0.1</i>	<i>0.01</i>	<i>0.8</i>	<i>1.5</i>	<i>0.2</i>	<i>0.3</i>	<i>0.03</i>	<i>1.6</i>
6	13	40.94	0.07	17.3	0.15	8.5	0.10	19	4.4	7.8	1.0	0.02	99.2
		<i>1.0</i>	<i>0.03</i>	<i>3.1</i>	<i>0.02</i>	<i>1.6</i>	<i>0.04</i>	<i>3.7</i>	<i>3.0</i>	<i>1.8</i>	<i>0.21</i>	<i>0.02</i>	<i>1.5</i>

no an. = number of analyses; in italics are 1 standard deviations.

Table 2. Microprobe analyses of pyroxene, olivine, nepheline, sodalite, and unidentified phase in the *Al3509* chondrule.

mineral	SiO ₂	TiO ₂	Al ₂ O ₃	Cr ₂ O ₃	FeO	MnO	MgO	CaO	Na ₂ O	K ₂ O	Cl	total	Fa	Fs	Wo
cpx	48.9	0.12	6.7	0.15	3.5	0.04	14.8	23.2	0.62	0.21	n.d.	98.3	–	5.9	50.0
cpx	45.6	0.03	11.0	0.12	5.9	0.04	12.0	24.0	0.31	n.d.	n.d.	99.1	–	10.2	52.8
cpx	47.1	0.07	11.6	0.12	4.8	0.09	11.7	23.4	0.70	n.d.	n.d.	99.5	–	8.6	53.9
nph	43.1	n.d.	35.7	n.d.	0.21	0.04	0.09	0.96	17.4	1.5	n.d.	99.0	–	–	–
ol	37.4	n.d.	0.27	0.10	24.7	0.16	36.6	0.09	0.12	n.d.	n.d.	99.5	27.5	–	–
ol	36.0	0.04	0.30	0.20	31.2	0.27	31.6	0.05	0.10	n.d.	n.d.	99.8	35.7	–	–
ol	35.1	n.d.	0.29	0.09	35.1	0.29	28.9	0.07	0.16	n.d.	n.d.	99.9	40.6	–	–
sod	39.1	n.d.	35.2	n.d.	0.18	n.d.	0.08	0.07	17.9	n.d.	7.1	99.6	–	–	–
un	29.9	0.05	11.1	0.12	30.5	0.25	26.4	0.27	0.19	0.04	0.02	98.9	–	–	–
un	30.9	0.08	8.7	0.11	30.5	0.22	27.0	0.24	0.20	0.04	0.03	98.0	–	–	–

cpx = high-Ca pyroxene; ol = olivine; n.d. = not detected; nph = nepheline; sod = sodalite; un = unidentified phase.

Table 3. Oxygen isotopic compositions of nepheline (nph), sodalite (sod), ferroan Al-diopside (px), ferroan olivine (ol), and unidentified phase (un) in the *Al3509* chondrule.

mineral	point #	$\delta^{17}\text{O}$	2σ	$\delta^{18}\text{O}$	2σ	$\Delta^{17}\text{O}$	2σ
px	1	1.5	1.0	8.0	0.7	-2.7	1.0
px	2	1.6	1.0	8.0	0.7	-2.6	1.0
px	3	2.0	1.0	8.4	0.7	-2.4	1.0
px	4	2.1	1.0	8.5	0.6	-2.3	1.0
nph	1	-0.8	2.2	3.4	1.9	-2.5	2.5
nph	2	-0.3	2.2	3.0	1.9	-1.9	2.4
ol	1	-2.9	2.1	0.4	1.2	-3.1	2.2
ol	2	-1.8	2.1	1.4	1.1	-2.5	2.2
sod	1	-1.9	2.1	-0.1	2.0	-1.8	2.4
sod	2	-2.8	2.2	1.0	2.0	-3.4	2.5
sod	3	-2.1	2.3	0.4	1.9	-2.3	2.5
sod	4	-2.8	2.3	0.8	2.0	-3.3	2.5
sod	5	-2.9	2.3	0.5	1.9	-3.1	2.5
un	1	0.1	1.9	2.8	1.2	-1.4	2.0
un	2	1.0	2.0	2.9	1.2	-0.5	2.1
un	3	-0.1	2.1	3.4	1.2	-1.9	2.2
un	4	-0.5	2.0	2.9	1.2	-2.0	2.1

Table 4. Aluminum-magnesium isotope compositions of sodalite and pyroxene in the *A13509* chondrule.

Mineral	$^{27}\text{Al}/^{24}\text{Mg} \pm 2\sigma$	$^{26}\text{Mg}/^{24}\text{Mg} \pm 2\sigma$
Pyroxene 1	0.9 ± 0.1	0.13939 ± 0.00028
Pyroxene 3	0.5 ± 0.1	0.13929 ± 0.00020
Sodalite 1	337 ± 36	0.1397 ± 0.0025
Sodalite 2	869 ± 96	0.1402 ± 0.0035
Sodalite 3	267 ± 45	0.1395 ± 0.0013
Sodalite 5	1453 ± 120	0.1407 ± 0.0032
Sodalite 6	455 ± 49	0.1389 ± 0.0011

Table 5. Chlorine-sulphur isotope systematics of sodalite in the *Al3509* chondrule.

Mineral	$^{35}\text{Cl}/^{34}\text{S} \pm 2\sigma$	$^{36}\text{S}/^{34}\text{S} \pm 2\sigma$
Al 3509 Sodalite		
#4	24140 ± 2404	0.00553 ± 0.00043
#6	3904 ± 528	0.00455 ± 0.00027
#7	1675 ± 152	0.00446 ± 0.00027
#8	4851 ± 486	0.00602 ± 0.00038
#9	62185 ± 5742	0.00473 ± 0.00085
Canyon Diablo Troilite		
CDT1	0.0022 ± 0.0006	0.003514 ± 0.000016
Terrestrial Sodalite		
Bahia 1	13812 ± 1246	0.00325 ± 0.00040
Bahia 13	10354 ± 935	0.00354 ± 0.00034
Bahia 16	13277 ± 1363	0.00287 ± 0.00064
Bahia 19	2113 ± 191	0.00304 ± 0.00019
Bahia 20	2198 ± 198	0.00339 ± 0.00016
Bahia 21	12819 ± 1162	0.00375 ± 0.00084
Bahia 22	16484 ± 1488	0.00405 ± 0.00035
Brevig 1	1289 ± 116	0.00333 ± 0.00008
Brevig 2	1206 ± 109	0.00344 ± 0.00011
Brevig 3	1169 ± 105	0.00340 ± 0.00012

FIGURE CAPTIONS

Figure 1. Maps using K_{α} x-ray emission of Mg (b), Ca (c), and Al (d), and a combined elemental map in Mg (red), Ca (green), and Al (blue) (a) of *Al3509*, Mann#1. The maps show that *Al3509* is rich in Al and Ca, but contains no identifiable Mg-rich phases, typically observed in Ca,Al-rich chondrules and CAIs (e.g., spinel, fassaite, forsteritic olivine, or low-Ca pyroxene). It shows radial chemical zoning (see Figs. 1c and 1d) and is surrounded by a thin fine-grained rim (FGR). The chemically distinct zones are numbered from 1 to 9 (see text for details). Region outlined in Fig. 1a is shown in Fig. 5a.

Figure 2. Maps using K_{α} x-ray emission of Mg (b), Ca (c), and Al (d), and a combined elemental map in Mg (red), Ca (green), and Al (blue) (a) of *Al3509*, Mann#2. This section is close to the end of the object and exposes only chemically distinct mantle zones 6–9. Although the same color scheme is used in Fig. 1a, there are clear differences in color of *Al3509*. These differences are an artifact of image processing using ENVI due to higher proportion of Type I chondrules in Fig. 1.

Figure 3. Maps using K_{α} x-ray emission of Fe (b), Na (c), and Cl (d), and a combined elemental map in Cl (red), Na (green), and Fe (blue) (a) of *Al3509*, Mann#1. The object is low in Fe and highly enriched in Cl and Na compared to the Allende matrix. The yellow and green colors in Fig. 3a correspond to sodalite and nepheline, respectively. The chemically distinct zones are numbered from 1 to 9 (see text for details). Region outlined in Fig. 3a is shown in Fig. 5a.

Figure 4. Map using K_{α} x-ray emission of Si (b), a combined elemental map in Cl (red), Na (green), and Fe (blue) (a), and backscattered electron images (c–f) of *Al3509*, Mann#2. The yellow and green colors in Fig. 4a correspond to sodalite and nepheline, respectively. This section is close to the end of the object and exposes only chemically distinct mantle zones 6–9. Regions outlined in Fig. 4a (from top to bottom) are shown in Fig. 4c and Fig. 4f, respectively. Regions outlined in Fig. 4c (from top to bottom) are shown in Figs. 4d and 4e, respectively. (b–e) The top region outlined in Fig. 4a is enriched in Si compared to the rest of the object and has a quenched, radial texture. It consists of skeletal crystals of sub-Ca pyroxene replaced by ferroan high-Ca pyroxene, and interstitial sodalite (sod) (Fig. 4e). In the peripheral part, these minerals are pseudomorphed by ferroan olivine (ol) and sodalite (sod) (Fig. 4d). (f) The mantle zones are crosscut by multiple veins composed of nepheline (nph), sodalite, and ferroan Al-diopside (cpx).

Figure 5. Backscattered electron images of a region in *Al3509*, Mann#1 outlined in Fig. 1a. The chemically distinct units (zones) are numbered from 1 to 9 in Fig. 5a. Figures 5b–d, e and g represent a traverse from the core to the edge of the object and illustrate the mineralogy of these zones. Figures 5f and 5h are from zones 8 and 9 in Mann#2, respectively. Regions outlined in Fig. 5b (from top to bottom) are shown in Figs. 5c and 5d. and = andradite; cpx = ferroan Al-rich high-Ca pyroxene; fgm = poorly-characterized fine-grained material; nph = nepheline; ol = ferroan olivine; sod = sodalite; un = unidentified mineral phase.

Figure 6. STEM and TEM images of FIB-prepared regions of the unidentified Mg-Al-Fe-rich phase (un) shown in Fig. 5. (a) Dark-field STEM Z-contrast image of FIB section of the unknown phase. Based on electron diffraction and EDS analysis the phase is ferroan olivine (Ol) with fine-scale intergrown lamellae of an Al-rich phase, probably chlorite. The image shows

three subparallel, elongate grains of olivine (Ol bright grain) embedded within a porous, inclusion-rich region of nepheline (Ne). The olivine grains show complex variations in Z-contrast due to the presence of intergrowths of a low-Z phase, nepheline (Ne) and voids which appear as nanometer-sized low-Z features distributed heterogeneously through the olivine. The platinum layer deposited to protect the sample during FIB sample preparation is the high-Z feature (Pt) in the lower part of the image. (b) Higher magnification Z-contrast image of a region at the interface between two of the olivine subgrains. The right hand region of the grain contains abundant, nanometer-wide lamellae of a secondary phase (black arrows) with higher Z-contrast, intergrown with the olivine (Ol). The distribution of the lamellae is heterogeneous within the olivine. Numerous nanometer-sized voids are also evident in the right hand grain. (c) Bright field TEM image of the olivine (Ol) grain shown in (b), but in a different orientation. The mottled contrast in the image is due to strain within the olivine lattice caused by the presence of subgrains and the intergrown lamellae of the secondary phase. A region of strain-free olivine on the rim of the grain is indicated by the white arrow. Thick lamellae of nepheline (Ne) which have undergone electron beam irradiation to form a porous amorphous material are present. (d) [011] zone axis electron diffraction pattern of olivine showing distinct asterism in electron diffraction maxima due to the strain within the olivine. The asterism is indicative of the presence of misoriented domains or subgrains within the olivine. Extra diffraction maxima are present (white arrow), between the (*h*00) diffraction maxima, indicating that the olivine is intergrown with a crystallographically oriented second phase. (e) Bright field TEM image showing the olivine in the second FIB section. The olivine (Ol) occurs as several subparallel, elongate grains with different widths intergrown with lamellae of nepheline (Ne). The large olivine grain in the center contains a heterogeneous distribution of elongate voids. The variable contrast within the grain is due to the presence of multiple subgrains separated by subgrains that appear to be decorated by subgrain boundary dislocations. (f) Higher magnification bright field image showing a detail of a region of strained olivine (Ol) containing abundant voids (white arrows). The voids in this region are subrounded and range from a few nanometers to 100 nanometers in size. Note the inclusion and strain-free rim on the edge of the olivine grain.

Figure 7. Selected area electron diffraction pattern of the [011] zone axis of olivine showing the presence of extra diffraction maximum between the (*h*00) diffraction rows, caused by the presence of the lamellae of the high-Z phase shown in Fig. 6b. The *d*-spacing of these diffraction maxima is 1.42 nm consistent with the (001) basal spacing of chlorite. The overall diffraction pattern of the second phase appears to be most consistent with a [100] zone axis of a chlorite phase. The patterns diffraction patterns show that the olivine and chlorite have a close crystallographic orientation relationship with $[011]_{\text{ol}}//[100]_{\text{chl}}$ and $(100)_{\text{ol}}/(001)_{\text{chl}}$.

Figure 8. Backscattered electron images of a fine-grained rim (FGR) and neighboring Allende matrix (MX) around *Al3509*, Mann-2 chondrule (chd). Region outlined in Fig. 8a is shown in Fig. 8b. The fine-grained rim is mainly composed of ferroan olivine (ol), nepheline (nph), and sodalite (sod). There are abundant rounded nodules of Ca,Fe-rich pyroxenes (Ca,Fe-px) in the Allende matrix just outside the fine-grained rim. The boundaries between the chondrule, fine-grained rim and matrix are indicated by dashed lines.

Figure 9. Backscattered electron images of the ferroan Al-diopside (a), sodalite (b, c), nepheline (d), ferroan olivine (e), and unidentified phase (f) measured for oxygen-isotope compositions. In Fig. 7a, regions sputtered during oxygen-isotope measurements are outlined. px = ferroan Al-diopside; nph = nepheline; un = unidentified phase; sod = sodalite.

Figure 10. Three-isotope oxygen diagram of ferroan Al-diopside (px), nepheline (nph), sodalite (sod), ferroan olivine (ol) and unidentified phase in *Al3509* (this study) and of secondary Ca,Fe-rich pyroxenes (px) and sodalite in the Allende matrix, rim around Allende CAI *TS24* (data from Cosarinsky et al., 2003), and Allende dark inclusion 3529 (data from Krot et al., 2000); error bars are 2σ . The terrestrial fractionation (TF) line and carbonaceous chondrite anhydrous mineral (CCAM) line are shown for reference. In Fig. 8b, the same data are plotted as $\Delta^{17}\text{O} = \delta^{17}\text{O} - 0.52 \times \delta^{18}\text{O}$. Oxygen isotopic compositions of all these phases plot along mass-dependent fractionation line with $\Delta^{17}\text{O}$ value of $\sim -2.5 \pm 0.5\text{‰}$ suggesting precipitation from a fluid of similar O-isotope composition. Locations of grains measured for oxygen isotopic compositions in *Al3509* are shown in Fig. EA1.

Figure 11. Aluminum-magnesium isotope diagram of sodalite and ferroan Al-diopside in *Al3509*.

Figure 12. Chlorine-sulphur isotope diagram of sodalite in *Al3509* and of terrestrial sodalite.

Figure EA1. Combined elemental maps in Cl (red), Na (green), and Fe (blue) (a) and in Mg (red), Ca (green), and Al (blue) (m) and backscattered electron images of *Al3509*, Mann#1 showing the locations of grains measured for oxygen isotopic compositions. Regions outlined in Fig. EA1a are shown in Figs. EA1b, e and g. Regions outlined in Fig. EA1b are shown in Figs. EA1c and d. Regions outlined in Figs. EA1e, g, i, k are shown in Figs. EA1f, h, j, and l, respectively. Regions outlined in Figs. EA1n are shown in Figs. EA1o and p. nph = nepheline; ol = ferroan olivine; un = unidentified phase; sod = sodalite.

Figure 1.

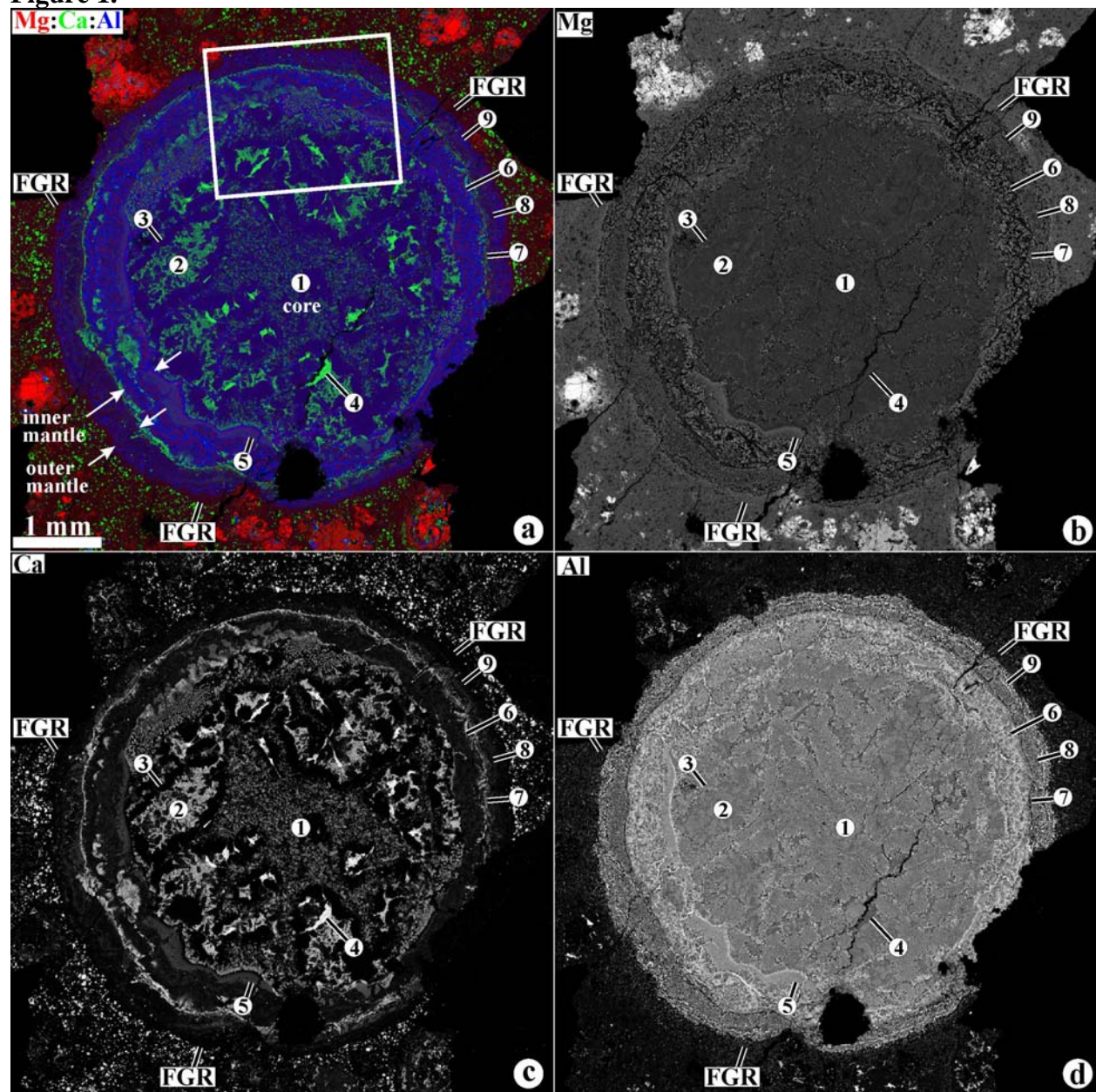


Figure 2.

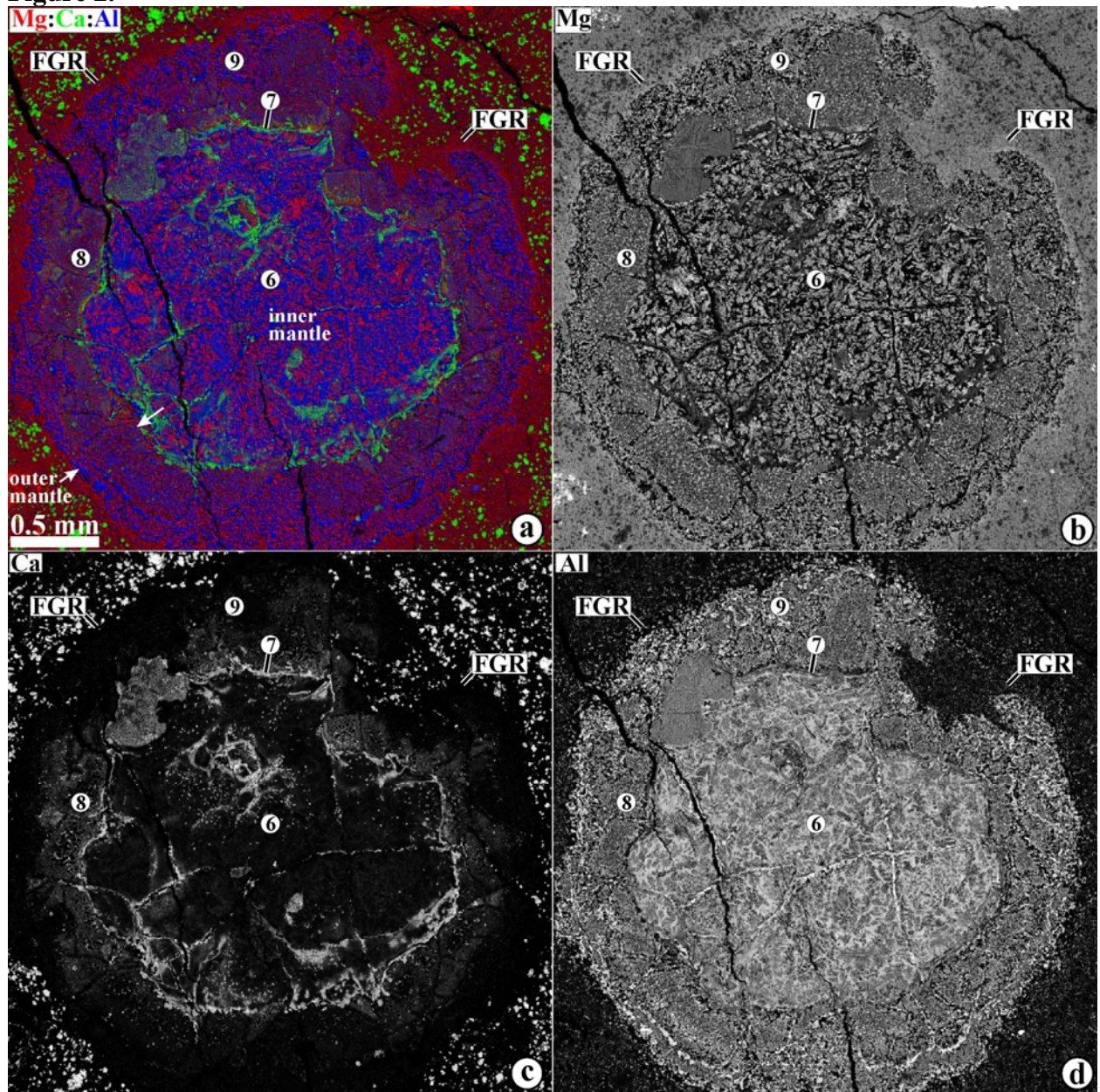


Figure 3.

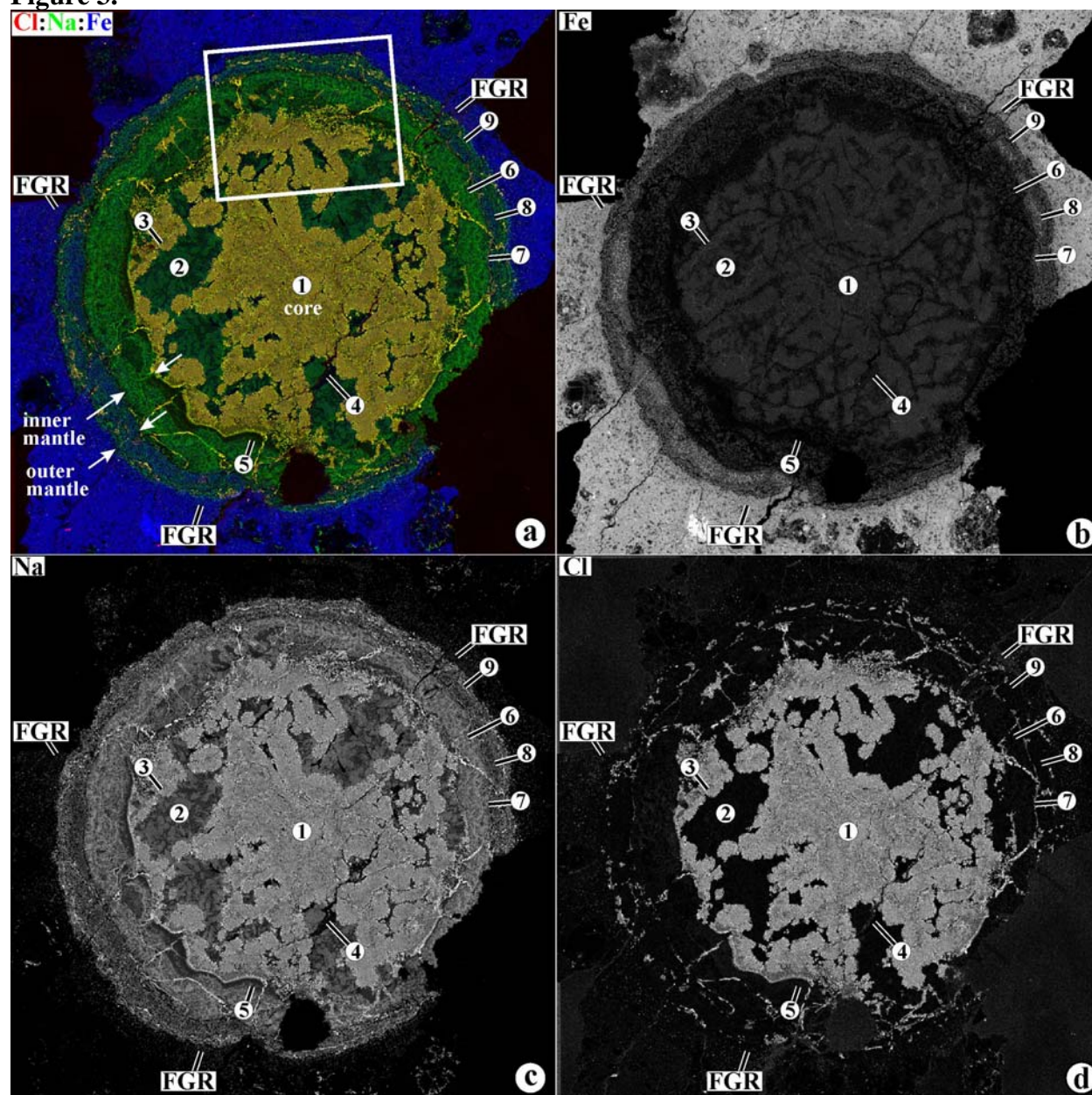


Figure 4.

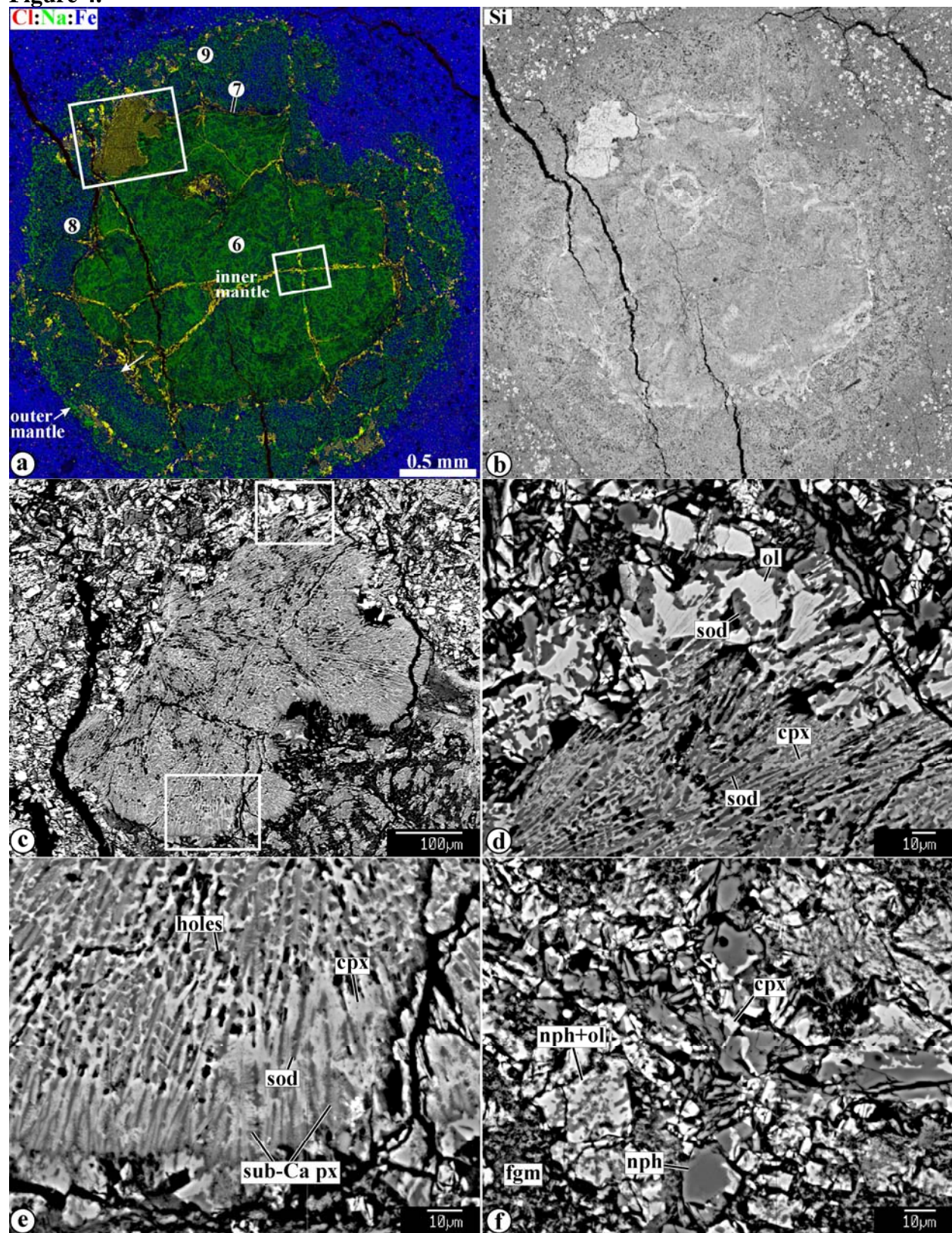


Figure 5.

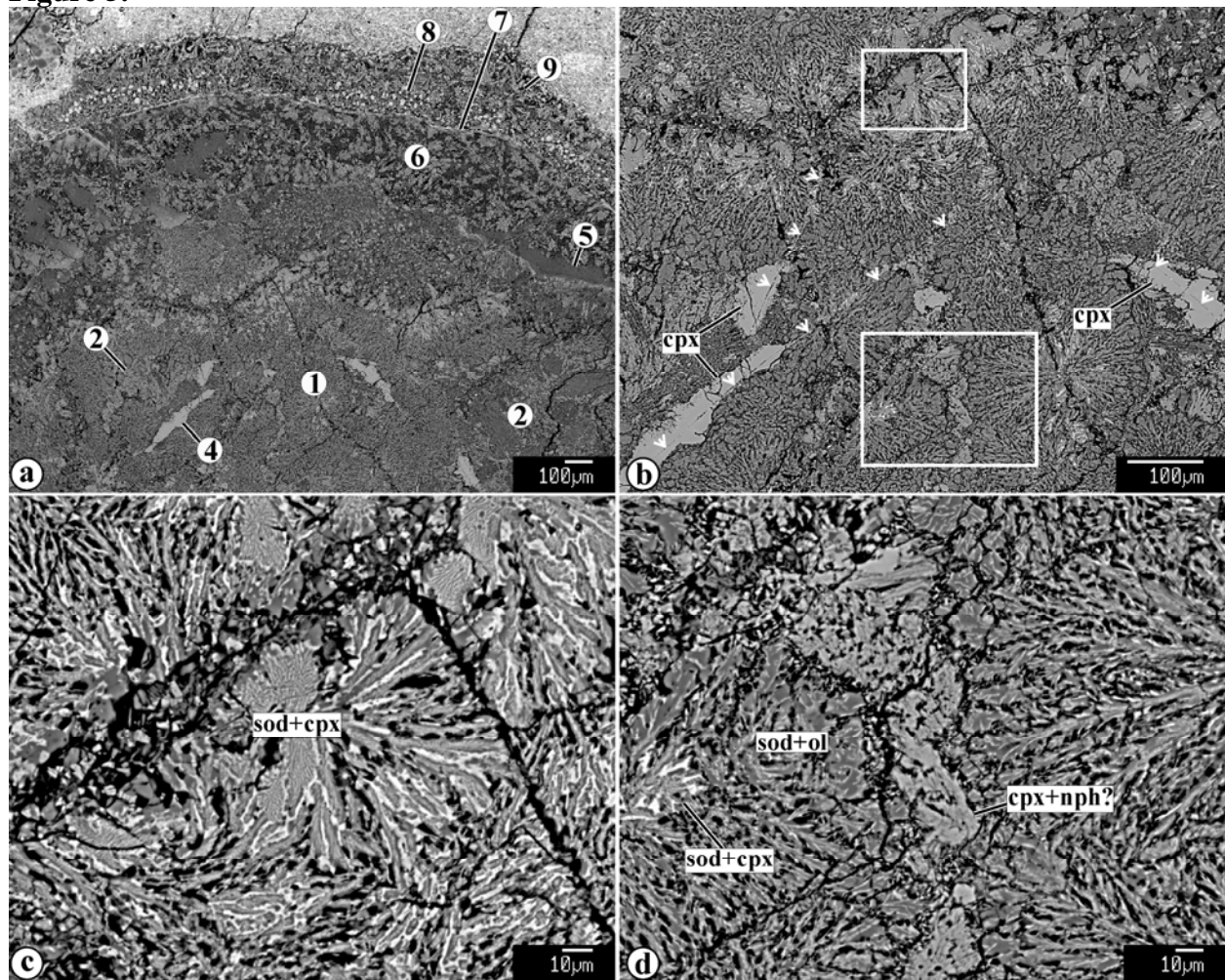


Figure 5 (cont.).

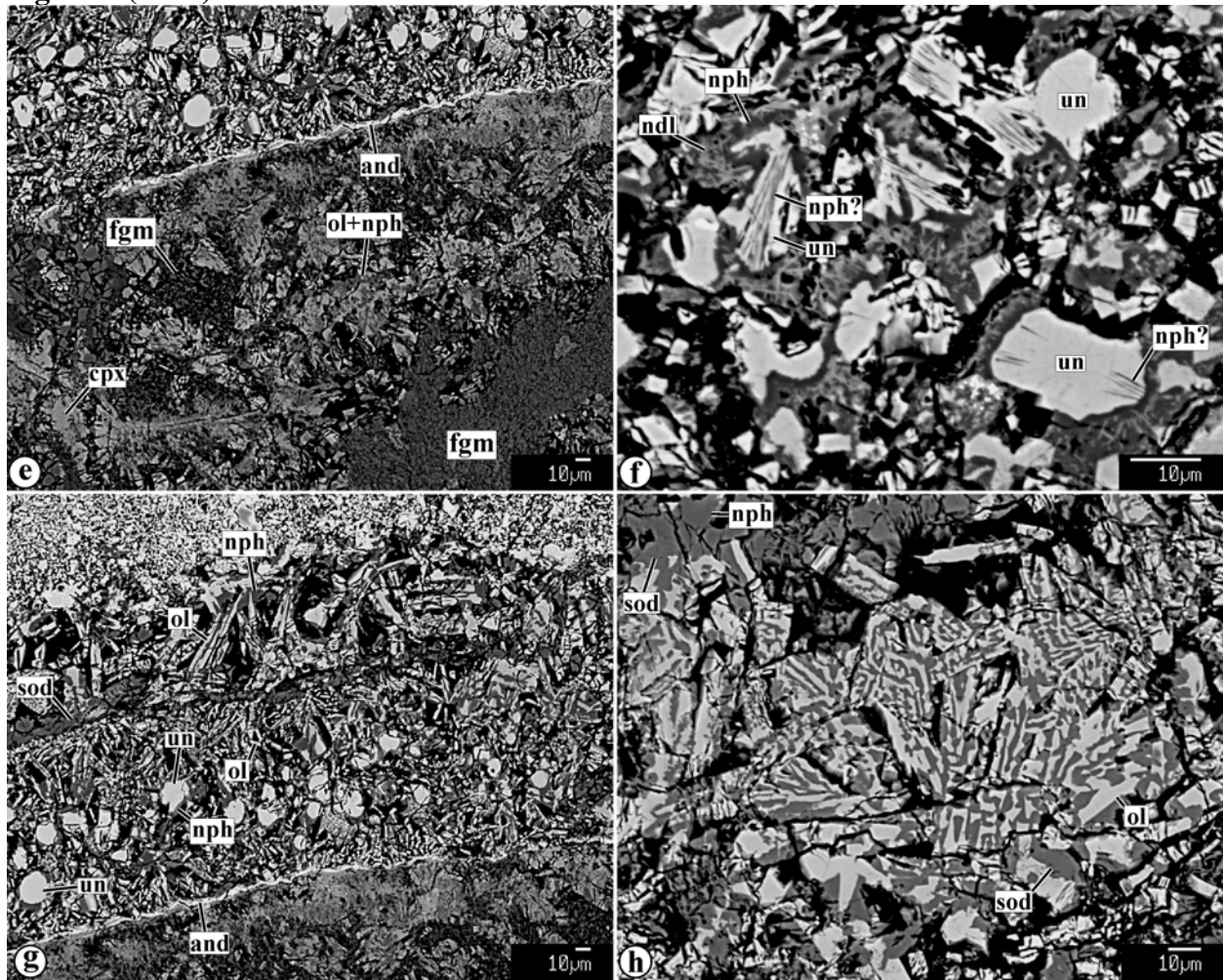


Figure 6.

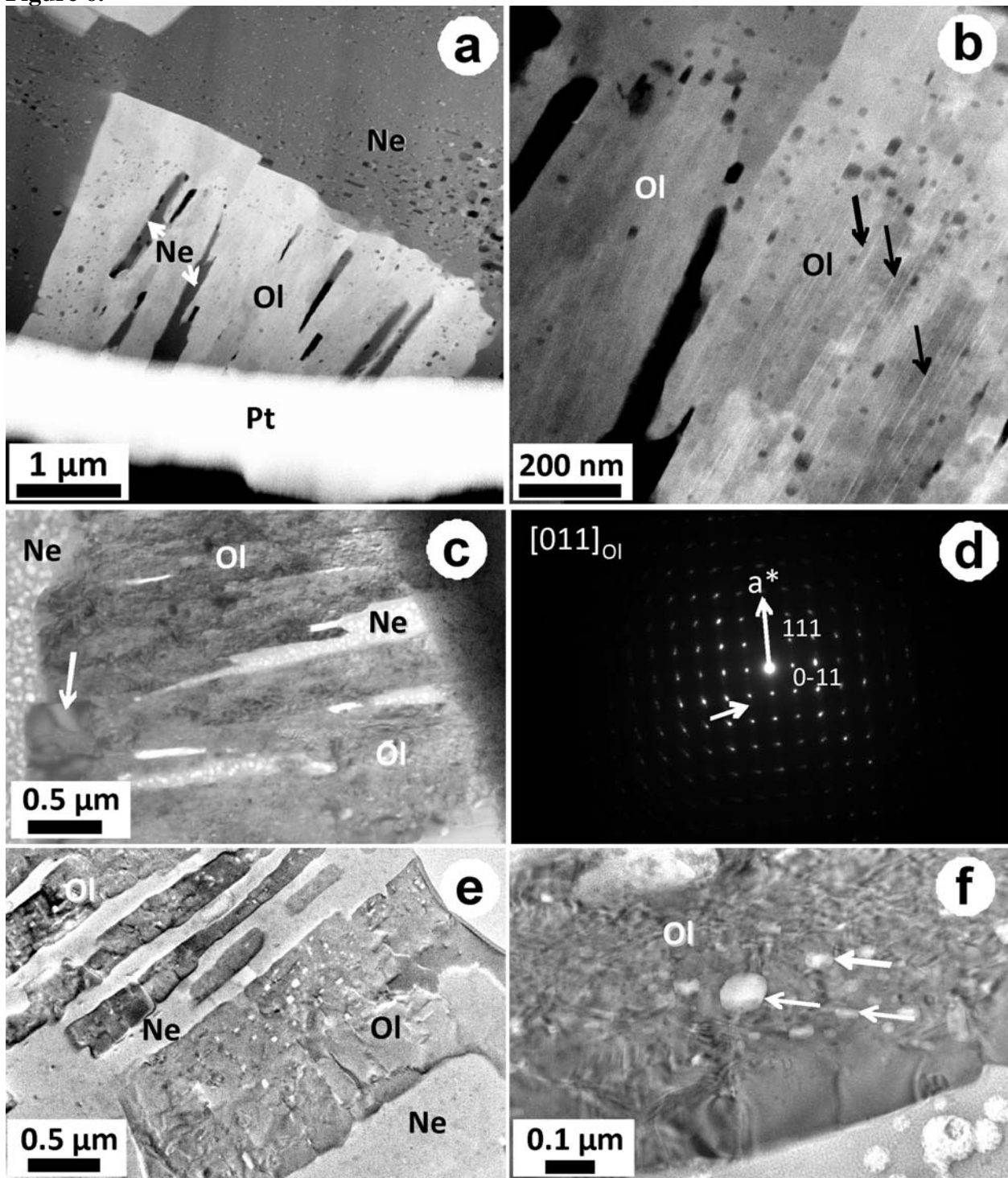


Figure 7.

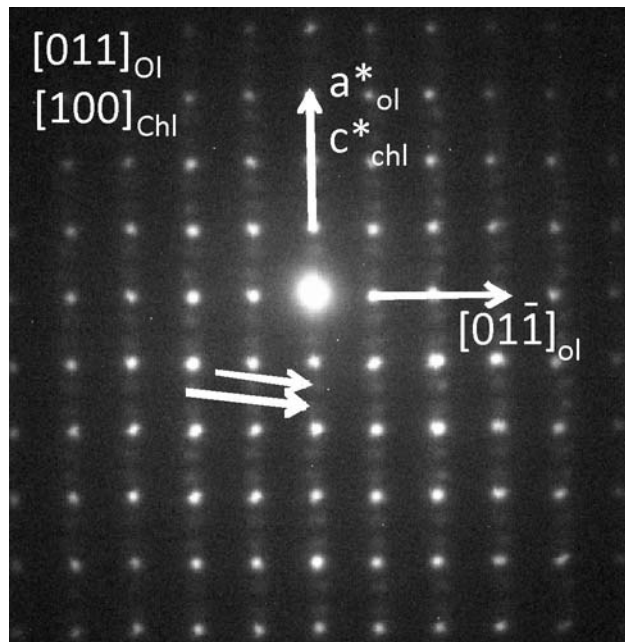


Figure 8.

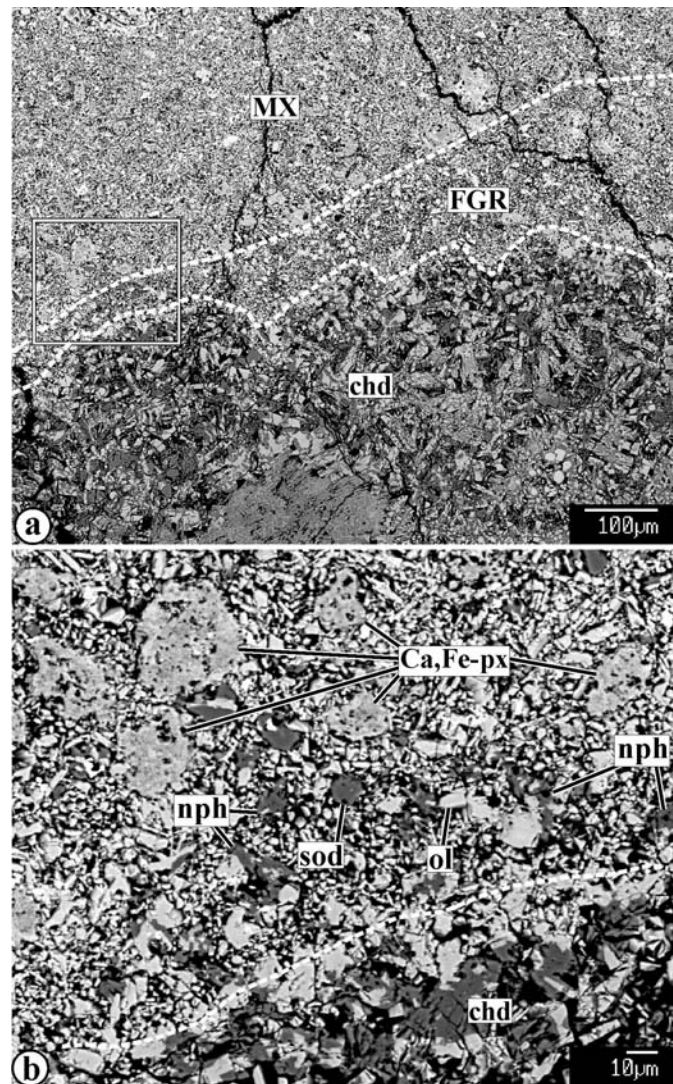


Figure 9.

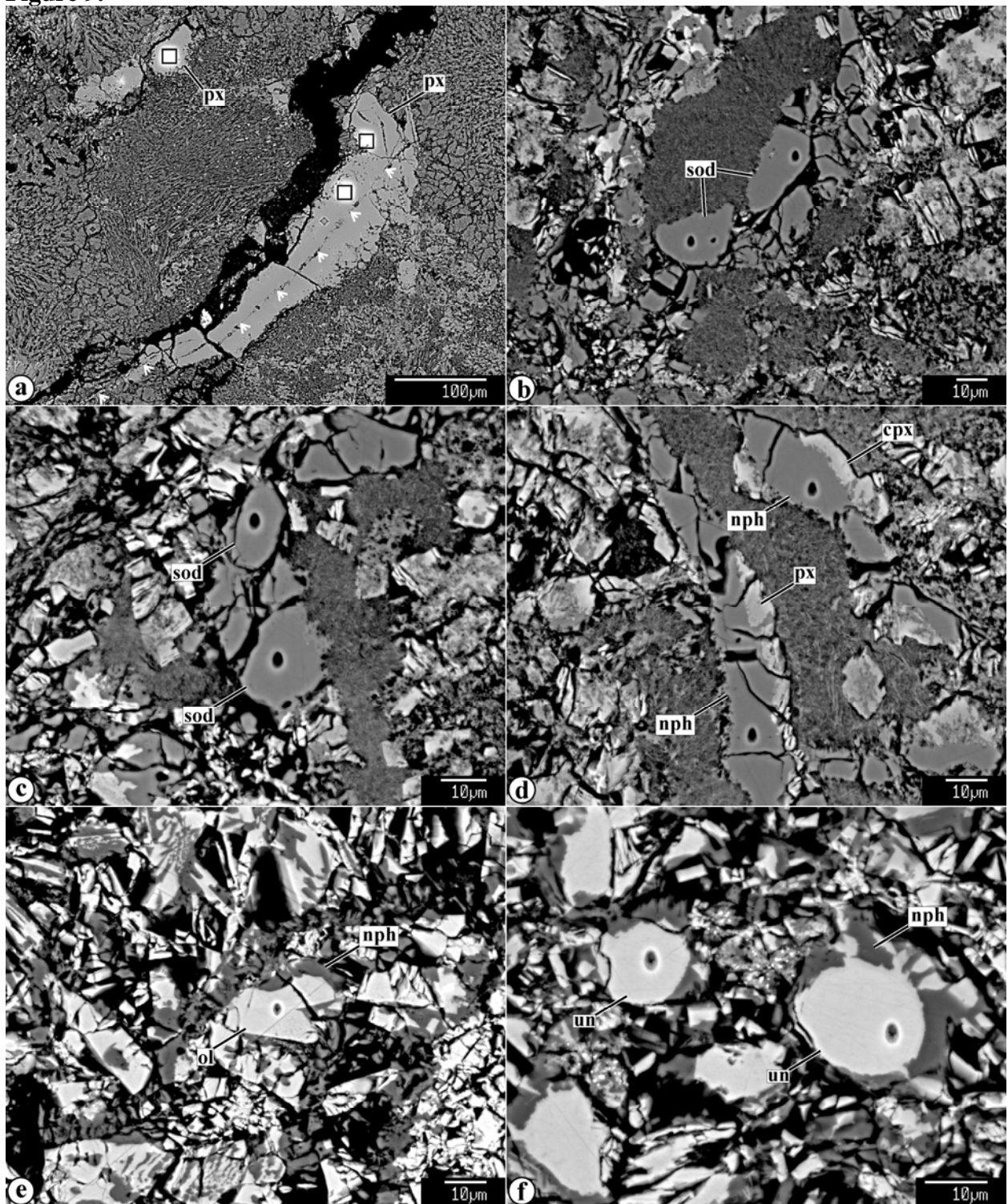


Figure 10.

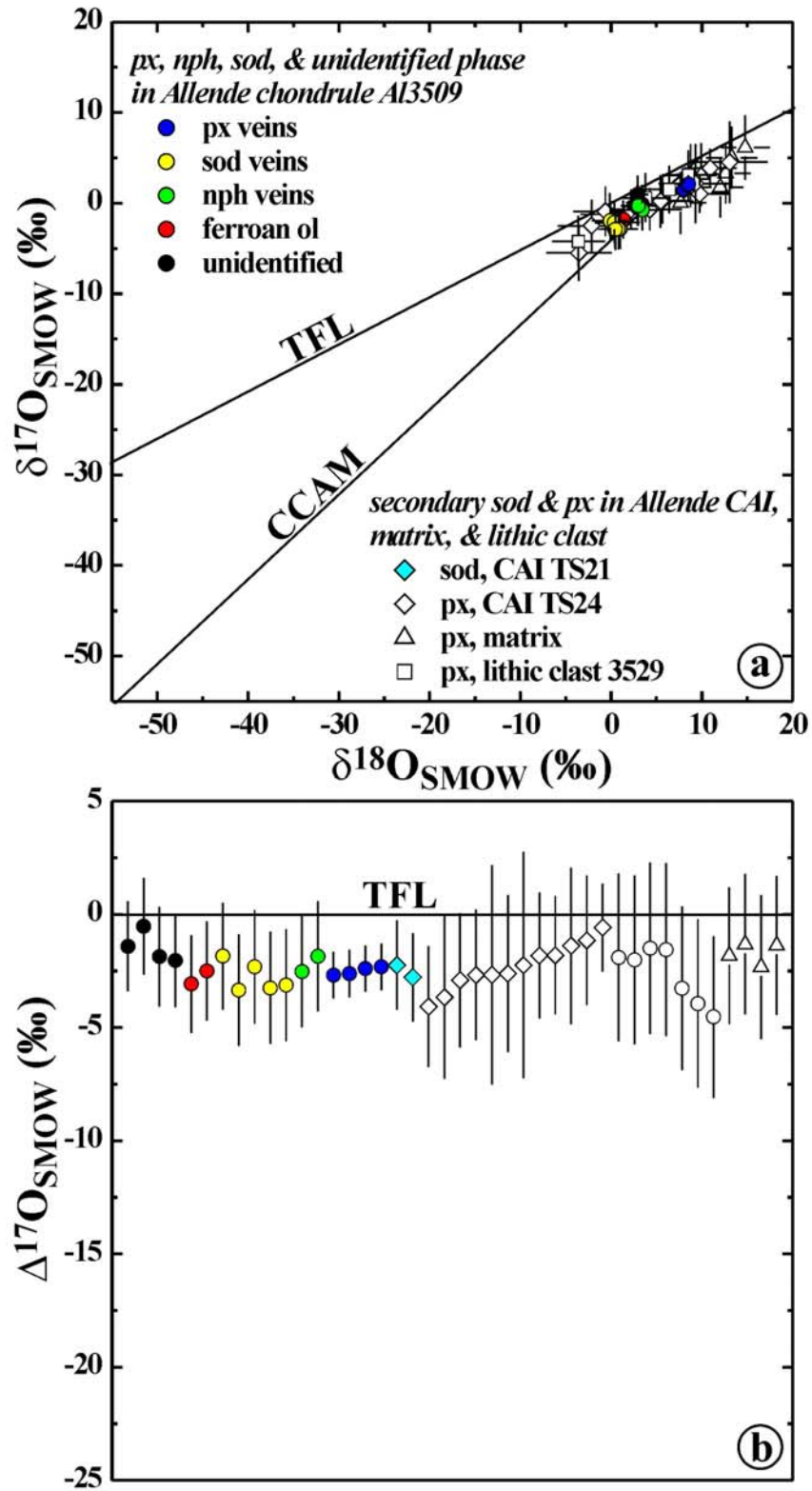


Figure 11.

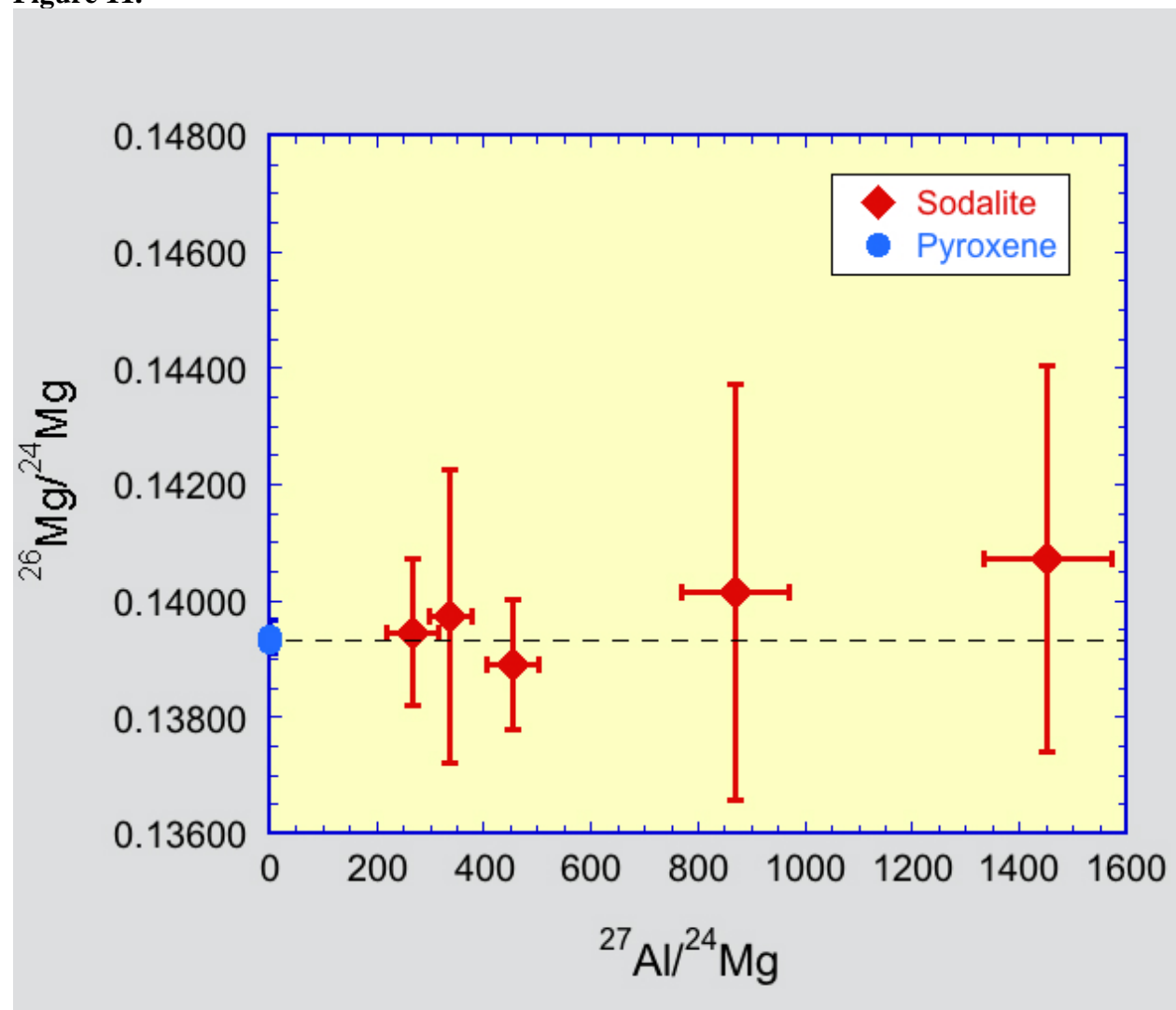


Figure 12.

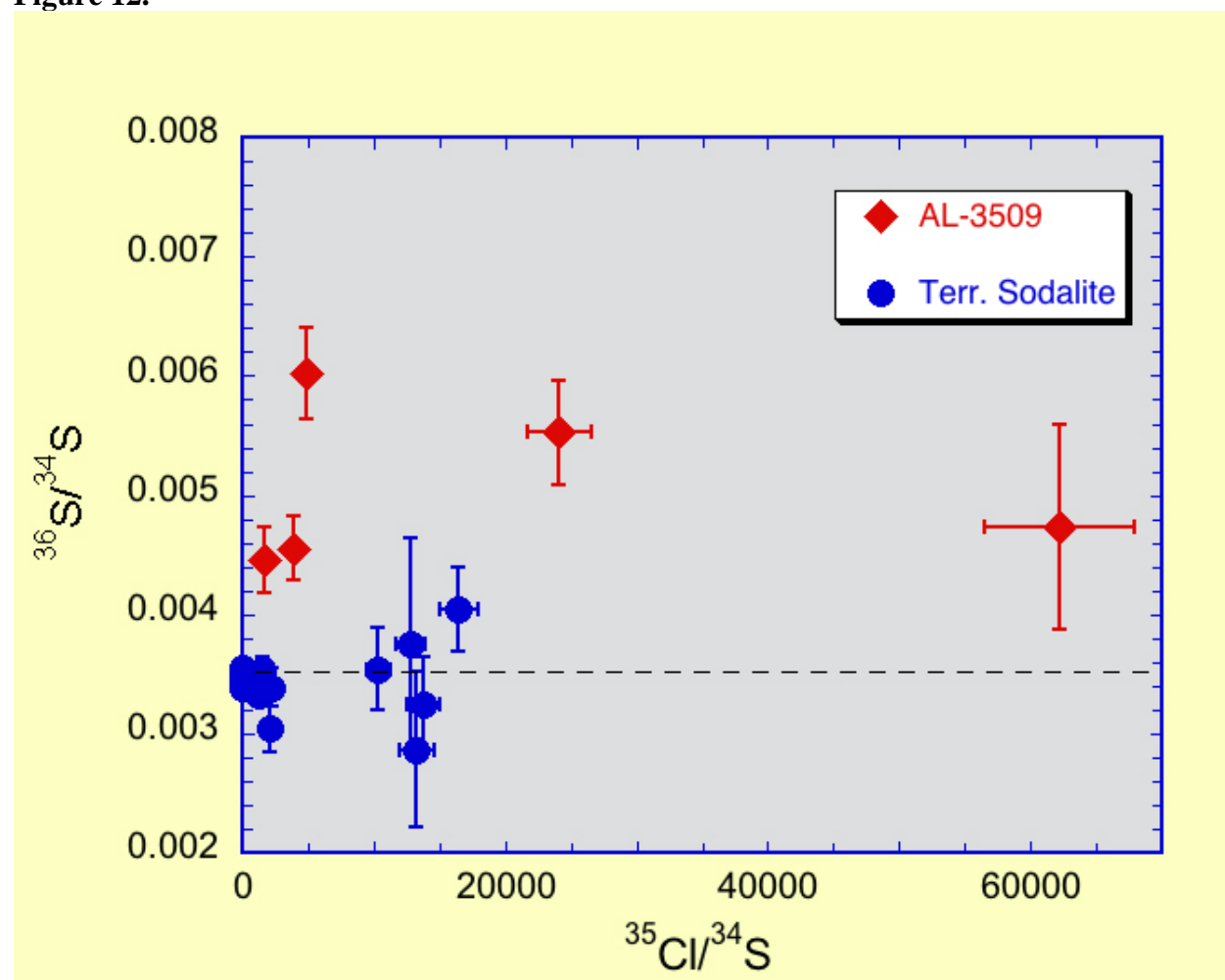


Figure EA1.

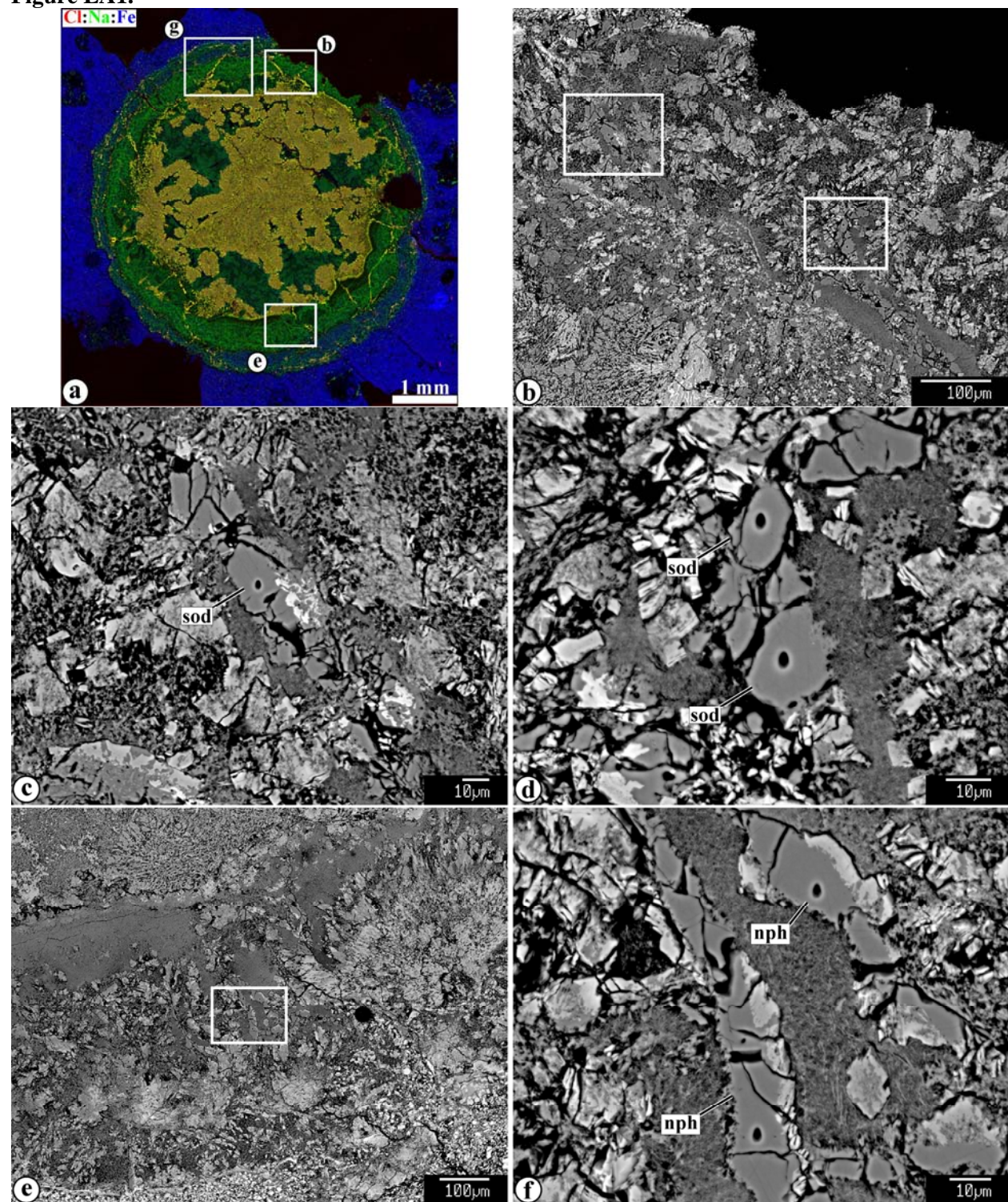


Figure EA1 (cont.).

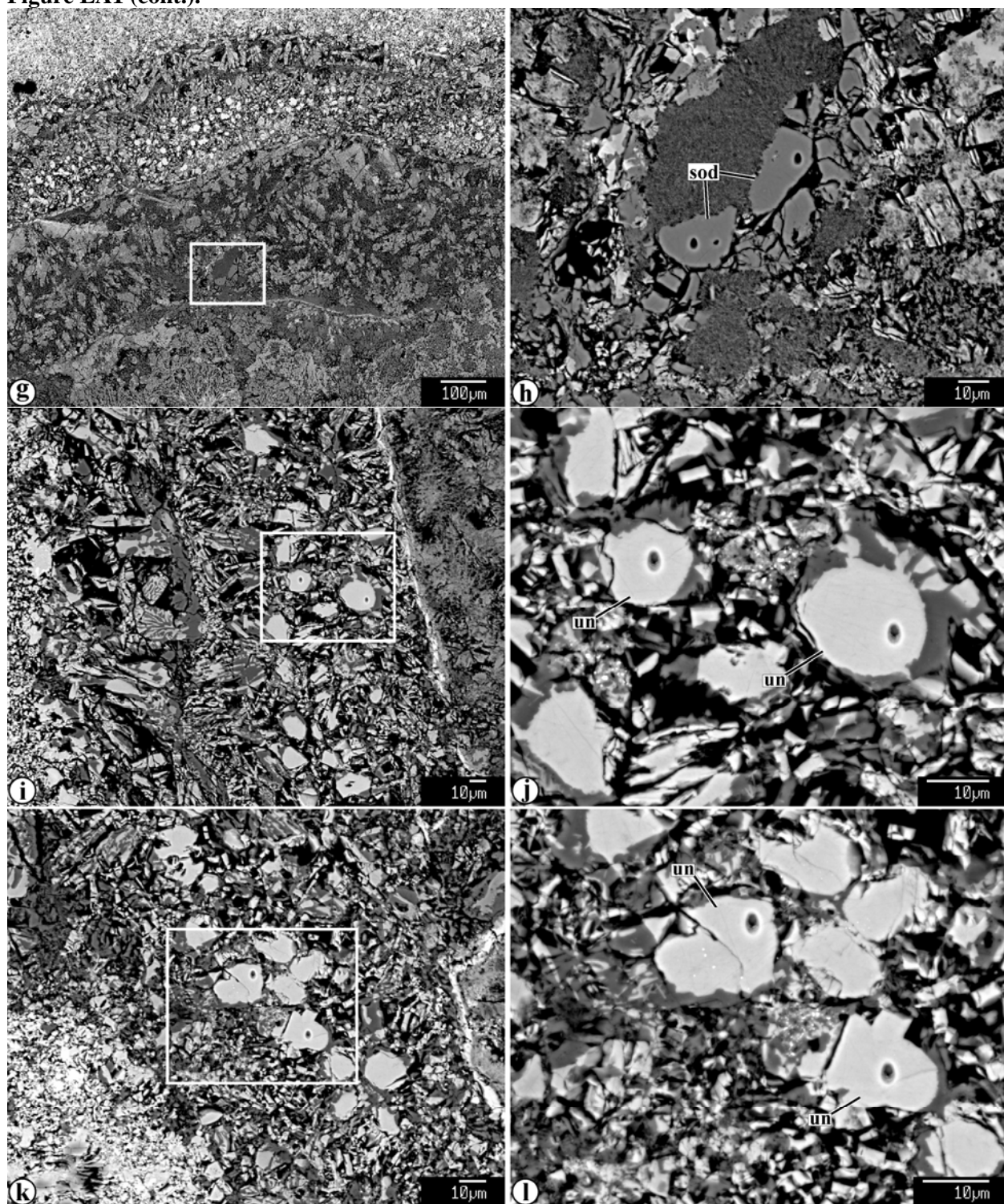


Figure EA1 (cont.).

